Science Advances
AAAS

Supplementary Materials for

The Winchcombe meteorite, a unique and pristine witness from the outer solar system

Ashley J. King *et al.*

Corresponding author: Ashley J. King, a.king@nhm.ac.uk; Luke Daly, luke.daly@glasgow.ac.uk

Sci. Adv. **8**, eabq3925 (2022)
DOI: 10.1126/sciadv.abq3925

This PDF file includes:

Materials and Methods

1. Fireball Observations

Fig. S1 shows example images of the Winchcombe fireball, which was detected by 16 of the stations operated by the UKFAll networks (Table S1). This makes the Winchcombe meteorite the most widely instrumentally observed carbonaceous chondrite fall to date.

1.1 *Trajectory*

The seven best optical records were used to measure the astrometric picks, with the remaining data having minor quality issues (e.g., unfavorable geometry, CCD blooming due to saturation, compression artefacts). Astrometric measurements were done in the SkyFit2 software using its radial distortion models (*34*), and the trajectory was computed using a Monte Carlo solver (*72*). Fig. S2 shows the fireball trajectory on a map in relation to the observing locations. Most cameras observed the fireball from within 100 km, the closest one being in Hullavington, which was able to accurately observe the details of final fragmentation due to its proximity and high optical sensitivity.

Fig. S3 shows the trajectory fit residuals. All stations had mean measurement errors below 100 m while the fireball was moving in a straight line, typically around 50 m, on par with previous instrumentally observed meteorite falls (*73, 74*). However, after the final fragmentation at a height of 35 km, the remaining fragments started deviating from a straight line. This is not a measurement error; the astrometric accuracy for the Hullavington GMN camera was 0.8 arc minutes (~15 m at the range of ~60 km to the fireball) based on 40 calibration stars selected across the field of view. This was the only camera sensitive enough to observe the end close enough to measure this deviation, thus, it was not possible to constrain the final fragment trajectory in three dimensions. A similar phenomenon has been reported for other fireballs (*75, 76*), but the cause of the deviation is currently unknown. All measurements below 35 km were excluded when computing the radiant

and the pre-atmospheric orbit. The calculated fireball radiant and the pre-atmospheric orbit are given in Table S2, and the physical and atmospheric trajectory information is given in Table S3.

1.2 *Dynamics and Fragmentation Modelling*

The unsaturated light curve up to magnitude -8^M was determined using SCAMP/FRIPON data to an accuracy of $\pm 0.1^M$. The brightest part of the light curve was measured on an unsaturated reflection in the optics of the Wilcot UKMON camera and adjusted to match the absolute calibration. The light curve and the dynamics were fitted using a meteoroid ablation and fragmentation model (*77*) and an improved luminous efficiency model (*78*). Fig. S4 shows the best fit, which was achieved using physical parameters appropriate for a carbonaceous body (*79*), and similar to those derived for the Maribo CM chondrite fall; meteoroid bulk density of ρ_M = 2000 kg m^{-3} and grain density of ρ_M = 3500 kg m^{-3} (*9*), intrinsic ablation coefficient σ = 0.005 kg MJ^{-1}, and the product of the drag and shape coefficient ΓA = 0.8.

The derived pre-atmospheric mass of 13 ± 3 kg is the smallest ever to be recorded for a carbonaceous chondrite by two orders-of-magnitude due to the low entry speed (13.5 km s^{-1}) relative to the associated fireballs of the other falls. Assisted by the shallow entry angle (~40°), the meteoroid slowly decelerated without reaching large dynamic pressures and disrupting the fragile body. The peak dynamic pressure of only 0.6 MPa is the lowest ever recorded for an instrumentally observed fall (*78*).

The observed part of the light curve above the height of 65 km is too faint compared to the model, even assuming no fragmentation. A smaller non-physical intrinsic ablation coefficient of σ = 0.002 kg MJ^{-1} better explains the observed light production; however, this is a known effect usually attributed to meteoroid pre-heating, which was not modelled in this work (*76*).

Three minor fragmentations occurred at pressures of 0.02 – 0.06 MPa, followed by a near-catastrophic 98% loss of mass into fragments at ~0.1 MPa. The subsequent dynamics could only

be explained by doubling the intrinsic ablation coefficient to $\sigma = 0.01$ kg MJ^{-1}. The remaining body did not show significant fragmentation until reaching 0.6 MPa at 35 km, upon which ~100 g of dust was released. This final fragmentation was evidenced by a bright peak, following which four individual fragments became visible in the Hullavington GMN video. The dynamic mass measurements indicated that they each had masses of ~100 g, consistent with the recovery of ~600 g of meteorite stones on the ground.

1.3 *Orbital Analysis*

To gain insight on the recent dynamical past of the Winchcombe meteoroid before it crossed the Earth's path, backwards integrations of the orbit were applied (*80*). 1090 orbital clones of the meteoroid were created based on the uncertainties (Table S2) and then integrated backwards using the Rebound IAS15 adaptive time step integrator (*81*) with the Sun + 8 planets + the Moon as active bodies. The state vector of the test particles was recorded every 1000 years, both in barycentric coordinates and as osculating ecliptic orbital elements. Backwards integrations were stopped at 3 million years in the past, way past the time for which meaningful dynamical insights of the meteoroid's history can be gained. Because the meteoroid was affected by Earth, Mars, and Jupiter in the past, the dynamical system is very rapidly chaotic. In post-analysis, the time at which each meteoroid clone entered near-Earth space (perihelion distance < 1.3 AU) was recorded. This gave a median near-Earth entry of ~80,000 years in the past, with 50% of the particles entering between 35,000 and 240,000 years. The median perihelion distance of the particles was also tracked; although the meteoroid probably spent time closer to the Sun than its impact perihelion distance suggests (~0.9868 AU), it most likely remained at > 0.7 AU throughout its history.

2. Recovered Samples

The first samples of the Winchcombe meteorite fall were found on the 1st March 2021 by the Wilcock family, who woke to discover a pile of dark powder on their driveway and fragments

scattered across the front lawn in the town of Winchcombe, Gloucestershire, UK. After seeing reports of the fireball in the media, Rob Wilcock picked up fragments while wearing rubber gloves and used a stainless-steel knife to collect the powder from the impact site. This material was then placed into visibly clean polypropylene pots and sealed polyethylene zip lock bags ~12 hours after the fall. Later the same day, a 17.2 g fragment was recovered using aluminum foil from a neighbor's driveway. The find was reported to UKMON on the 1st March 2021, and on the 3rd March Richard Greenwood from the Open University visited the Wilcock family and confirmed the meteorite fall. Further material was collected from the driveway and lawn over the next four days using powder-free nitrile gloves, aluminum foil, glass vials and polyethylene sample bags.

The freshest material was transferred to the Natural History Museum (NHM), London on the 4th March 2021 and then weighed and curated on the 5th March 2021. The largest fragments (~ > 2.5 g) were wrapped in high purity aluminum foil and stored in acid free trays with Revolutionary Preservation K (RP-K) oxygen scavengers within Escal enclosures. Smaller fragments and powder were sealed in glass vials stored within polyethylene sample bags.

In the week following the fall, samples of the Winchcombe meteorite were also found on properties in the village of Woodmancote, which lies ~4 km to the west of Winchcombe. The largest individual piece of the Winchcombe meteorite is a 152.0 g fusion-crusted stone, which was recovered on the 6th March 2021 by Mira Ihasz, a member of a team from the University of Glasgow, from farmland between Winchcombe and Woodmancote. The stone, handled and initially stored using nitrile gloves and geological sample bags, was embedded in the damp soil, and split into two pieces (48.9 g and 103.1 g) during extraction, revealing a dark interior with few visible white flecks.

In total, 531.5 g of the Winchcombe meteorite was recovered less than seven days after the fall. During that week, the weather in the local area was stable and mainly cloudy; the maximum

daytime temperature was 9 °C and there was no rainfall, although the humidity was high and there was heavy fog and dew on the ground. Over the next four weeks a further 70.4 g of material from the strewn field was recorded, giving the Winchcombe meteorite a total known mass of 601.9 g. Table S4 summarizes the recovered meteorites and Table S5 gives details about the samples analyzed in this study.

3. Reflectance Spectroscopy

Fig. S6 (a) shows that the Winchcombe meteorite samples have red spectral slopes (increasing reflectance with increasing wavelength) that could be related to particle size (*82*). As both samples were prepared in the same way, slight differences in the spectral slope can be attributed to the composition and/or abundance of phyllosilicates (~88 and 93 vol%, Table S13; (*83*)). Fig. S6 (b) shows a strong feature near 2.7 μm attributed to Mg-rich phyllosilicates and OH^-/H_2O, while the shoulder near 3 μm for sample 1b-38 could be related to a higher content of iron or water. These, and other subtle features in this spectral region, are likely related to parent body aqueous alteration and adsorbed terrestrial moisture.

The MIR region contains features due to the fundamental vibrations directly caused by the structure and chemistry of the bulk mineralogy. Fig. S6 (c) shows a Christiansen feature (CF) near 9 μm consistent with low silicate polymerization. A small shift in the position of the CF to longer wavelengths for BM.2022,M1-91 correlates to the slightly higher olivine abundance in this sample (Table S13).

4. Neon Isotopic Composition

Neon data are given in Table S6. As is common for carbonaceous chondrites, the bulk of the Ne originates from trapped components rather than produced from galactic cosmic rays during recent exposure in space. High $^{20}Ne/^{22}Ne$ are present in the low temperature steps of both samples, which records the release of solar wind (SW) derived Ne, indicating either the presence of regolith

material or the preservation of primordial material that was irradiated prior to accretion. The low $^{20}Ne/^{22}Ne$ of the higher temperature steps indicates that both samples contain appreciable contribution of pre-solar Ne (Ne-Q; (*84*)) and Ne-HL (*85*).

The isotopic composition of the total Ne released from each stone are plotted as circles on Fig. S7. They demonstrate that pre-solar Ne dominates in BM.2022,M4-7 and solar wind dominates in BM.2022,M2-36. The concentration of cosmogenic ^{21}Ne ($^{21}Ne_{cos}$) was determined from the measured Ne content and isotope composition and the trapped endmembers defined by (*15*). The range of $^{21}Ne_{cos}$ production rates (P_{21}) used for the calculation of cosmic-ray exposure (CRE) ages (1.24 – 3.08 × 10^{-8} cc/g/Ma) were determined using the models for carbonaceous chondrites developed by (*86*) and mean bulk chemical composition of CM chondrites from (*87*). We assume a pre-atmospheric meteoroid radius of 10 cm to 65 cm. Using the range of P_{21} CRE ages are 0.09 – 0.21 Ma for BM.2022,M2-36 and 0.06 – 0.15 Ma for BM.2022,M4-7. This is within the main CRE cluster of CM chondrites (*15*).

5. Cosmogenic Nuclides

Several gamma-lines were identified in the gamma-ray spectra of the analyzed meteorite fragments (122.06 keV (^{57}Co), 477.60 keV (^{7}Be), 810.77 keV (^{58}Co), 834.84 keV (^{54}Mn), 846.76 keV (^{56}Co), 889.28 and 1120.54 keV (^{46}Sc), 1173.24 and 1332.50 keV (^{60}Co), 1274.5 keV (^{22}Na), and 1808.65 keV (^{26}Al). The corresponding half-lives of these cosmogenic radionuclides are ranging from 53.22 days (^{7}Be) to 0.717 Ma (^{26}Al). AMS identified another long-lived radionuclide, ^{14}C (half-life of 5730 a). Table S7 gives results of the analyses of cosmogenic radionuclides in the Winchcombe meteorite samples. Generally, a reasonable agreement has been obtained between the gamma-spectrometry laboratories, showing results within statistical uncertainties.

Cosmogenic radionuclides found in meteorites are products of interactions of cosmic-ray particles of galactic and solar origin with the meteoroid bodies. Galactic cosmic rays because of

higher energies produce in meteoroids secondary and higher generations of neutrons and protons, which then in interaction with target nuclei produce cosmogenic radionuclides, which can be used to study the origin and characteristics of meteorites (e.g., their dimensions, CRE ages, orbits in space), as well as temporal and spatial variations of cosmic rays.

The dominant cosmogenic radionuclides present in the Winchcombe meteorite are ^{7}Be, ^{54}Mn and ^{22}Na. Other measured radionuclides (^{46}Sc, ^{26}Al, ^{56}Co) were produced in much smaller quantities. The important observation is the presence of short-lived radionuclides (^{7}Be, ^{56}Co, and ^{46}Sc), which clearly demonstrates that the analyzed fragments originated from the recent Winchcombe meteorite fall.

When comparing the measured radionuclide activities in the Winchcombe meteorite with other carbonaceous chondrites, the observed activities were much smaller. For example, in the Maribo CM chondrite, the levels of ^{7}Be, ^{26}Al and ^{60}Co were several times higher, reflecting different production scenarios. A small dispersion in activities of the samples presented in Table S7 indicates that the positions of the samples in the meteorite body were close to each other.

The ^{22}Na and ^{26}Al radionuclides were produced mainly by secondary neutron and proton reactions with energies > 10 MeV on target nuclei of Si, Al and Mg. For other radionuclides, except for ^{60}Co and ^{14}C, the main target was Fe. The measured activities depend on the flux of cosmic-ray particles, nuclear reaction cross sections, the concentration of the main target element in the meteorite, and the position of the fragment in the meteorite body. As ^{22}Na and ^{26}Al were produced in similar nuclear reactions, their activity depth profiles should be similar, and their activity ratio, ^{22}Na/^{26}Al should not depend on shielding effects in the meteorite. The observed ^{22}Na/^{26}Al activity ratio in the Winchcombe meteorite was 5.50, much higher than in the case of Maribo (1.79), and higher than the value of 1.5 averaged over a solar cycle by (*88*) for chondrites. The high ^{22}Na/^{26}Al activity ratio has been caused by unsaturated production of ^{26}Al.

A specific case is ^{60}Co, which is produced predominantly by the thermal-neutron capture reaction ^{59}Co (n, γ) ^{60}Co. ^{60}Co is one of the most suitable radionuclides for the determination of the position of samples within the meteorite body and for calculating its pre-atmospheric radius (*89*). Unfortunately, only a detection limit for ^{60}Co was estimated (< 8 dpm kg^{-1}), which would indicate that the analyzed fragments were located on the meteorite surface, and its size was too small for the development of a nucleonic cascade.

The absence of ^{60}Co in the analyzed Winchcombe meteorite indicates either a small concentration of the target isotope (^{59}Co) in the meteorite and/or its small radius. The cobalt concentration in two Winchcombe samples was measured to be 526 and 521 ppm (Table S7), which is lower by about 10% than the mean concentration in CM chondrites (*90*). After appropriate corrections for chemical composition, and following the approach of (*91, 92*), the pre-atmospheric radius of the Winchcombe meteorite is calculated as < 20 cm.

The measured ^{14}C activity in a small sample was 13.3 ± 0.4 dpm kg^{-1} (Table S7), and after corrections for chemical composition (*92*), the radius is 5 ± 3 cm. The measured ^{14}C activity in the Winchcombe is lower at least by about a factor of two when compared with other chondrites, which could be due to the high-water content in the meteorite, which changes the distribution of thermal neutrons by elastic scattering on hydrogen. Therefore, the ^{14}C-derived radius could be lower by about a factor of two.

^{26}Al can also be used to estimate the pre-atmospheric radius of the Winchcombe meteorite, although its activity is very low due to its short exposure age. A comparison of the saturated ^{26}Al activity in the meteorite with Monte Carlo simulations of ^{26}Al production rates in (*86*), after appropriate corrections for its chemical composition, suggest that the pre-atmospheric radius of the Winchcombe meteorite was 15 ± 5 cm. Using the measured bulk Winchcombe meteorite

density of 2100 kg m^{-3}, the initial mass of the meteoroid is estimated to be 30 ± 10 kg, in a reasonable agreement with the fireball observations.

The CRE ages of the Winchcombe meteorite was calculated using the method of (*93*) using only ^{26}Al data (*94*) and equation:

$$A = P (1 - e^{-\lambda T}),$$

where A is the cosmogenic radionuclide activity, P is its production rate in the meteorite by cosmic-ray particles, λ is the decay constant, and T is the time of the meteorite irradiation equal to its CRE age. Fig. S8 shows saturated ^{26}Al production rates, estimated for different radii of the Winchcombe meteorite (following the Monte Carlo model of (*86*)), adjusted for its chemical composition. Using the corresponding production rates of 32 and 39 dpm kg^{-1}, the CRE ages are 0.29 Ma and 0.24 Ma, with an average value of 0.27 ± 0.08 Ma. This value is in good agreement with ^{21}Ne based value presented in this work (0.3 Ma) (Section 4).

6. Bulk Element Abundances

The final meteorite abundances are given in Tables S8 and S9 and are consistent with the range for CM chondrites (e.g., *90*).

7. Oxygen Isotopes

Table S10 summarizes the results of the oxygen isotope analysis of the Winchcombe meteorite. Sample BM.2022,M1-85 yielded a composition of $\delta^{17}O$ = 2.75 ‰, $\delta^{18}O$ = 9.48 ‰, and $\Delta^{17}O$ = 2.18 ‰, while sample BM.2022,M1-86 gave values of $\delta^{17}O$ = 0.94 ‰, $\delta^{18}O$ = 7.29 ‰, and $\Delta^{17}O$ = 2.85 ‰. These compositions are consistent with classification of the Winchcombe meteorite as a CM chondrite.

8. Titanium Isotopes

Table S11 gives the Ti isotopic composition of the Winchcombe meteorite. The values are in good agreement with previous analyses of CM chondrites reported in the literature.

9. Chromium Isotopes

Table S12 gives the Cr isotopic composition of the Winchcombe meteorite, and Fig. S9 shows that the combined Cr and Ti isotopic values are in good agreement with previous analyses of CM chondrites reported in the literature.

10. X-ray Diffraction

Fig. S10 shows the scanning XRD pattern of the Winchcombe meteorite, which is typical of CM chondrites. Intense peaks at ~14° and ~29° and a broader feature at ~23° are attributed to abundant Fe- and Mg-bearing serpentines, while other minor phases identified from the pattern include olivine, magnetite, pyrrhotite, calcite and tochilinite.

The bulk mineralogy of the Winchcombe meteorite is summarized in Table S13. The most abundant phases were Fe- and Mg-bearing serpentines, with little difference found between the three analyzed samples (87 – 93 vol.%). Similarly, each sample contained a much lower abundance (3.1 – 8.1 vol.%) of anhydrous silicates (olivine and enstatite). From these abundances, the phyllosilicate fractions (PSF = total phyllosilicate abundance / [total anhydrous silicate + total phyllosilicate abundance]) were calculated as 0.92 – 0.97, giving petrologic types of 1.2 – 1.1 on the alteration scale of (*95*). The bulk mineralogy of the Winchcombe meteorite is therefore consistent with highly altered CM chondrites.

11. Petrographic Observations

A total area of 154.2 mm^2 across the 14 polished sections of the Winchcombe meteorite was characterized by SEM-EDS. In general, the sections were found to be typical of CM chondrites, consisting of chondrules, calcium-aluminum-rich inclusions (CAIs) and phyllosilicate clumps and/or tochilinite-cronstedtite intergrowths (TCIs), set within a matrix of finer-grained

phyllosilicates, carbonates, Fe-sulfides, and magnetite. Many of the coarse refractory objects retain well preserved fine-grained rims (FGR).

Petrographic observations indicate that the Winchcombe meteorite is a breccia containing multiple lithologies (Fig. S11). The main lithology in the Winchcombe meteorite accounts for >50 % of the area analyzed in this study. In this lithology, chondrules are near-complete pseudomorphs, with most of their interiors replaced by Fe- and Mg-bearing phyllosilicates (Fig. S12 (a)). Anhydrous Mg-rich (Mg# >97) primary silicate minerals remain in ~20 % of the chondrules or occur as isolated grains (<2 area%, up to ~200 μm in length) in the matrix (Table S16). These show evidence for etching, dissolution, and corrosion, although some still retain enclosed Fe-Ni metal grains.

A small number of chondrules (<3 %) in the main lithology are calcitized (Fig. S12 (b)). These chondrule pseudomorphs, the main occurrence of carbonate in this lithology, are similar to the type 2 grains reported by (*96*). The compositions of the carbonates are relatively pure $CaCO_3$ with minor Mg (<3.0 wt.%) and Fe (0.3 – 3.3 wt.%) and trace Mn (Table S15). Intact CAIs are rare, with most showing replacement by carbonates and retaining only residual primary silicate minerals (Fig. S12 (c) and (d)).

The matrix comprises >80 area% of the main lithology and is dominated by a series of coarse, usually rounded to sub-rounded, phyllosilicate clumps with fibrous, porous, or meshwork textures that range in size from ~20 – 70 μm (Fig. S13). The cores of some clumps are Fe-rich (Mg# 36 – 61) and appear relatively homogenous in BSE images, while others have bimodal structures with Mg-enriched cores (Mg# 73 – 79) and Fe- and S-rich (avg. S = 4.4 at.%) rims (Table S15). The rims are fibrous with needle-like radiating acicular grains that extend into the core of the clump. In many examples, three or more phyllosilicate clumps occur in close proximity to form a single larger rounded object (Fig. S13 (b)). The phyllosilicate clumps are enclosed by

finer-grained matrix materials that are darker in BSE images (Mg# 65 – 76). The matrix contains Ni-rich (24 – 34 wt.%) pentlandite with euhedral rounded or lath-shaped grains up to ~100 μm in size (Table S15), but magnetite was not observed.

The main lithology in the Winchcombe meteorite experienced a high degree of parent body aqueous alteration, which is reflected in the extensive replacement of chondrule silicates and metal, including the absence of any glassy mesostasis, the presence of type 2 calcite grains, the low FeO/SiO_2 and S/SiO_2 ratios of phyllosilicate clumps, and high Mg-content of the fine-grained matrix. Its mineralogical, chemical, and textural properties are consistent with a petrologic subtype of CM2.1.

Other lithologies in the Winchcombe meteorite were found to contain phyllosilicate clumps, TCIs, and multiple generations of calcite (Fig. S14). Several also have Mn-bearing dolomite, Fe-sulfides (usually pentlandite but pyrrhotite was also identified), magnetite framboids and platelets, and unusual, rounded grains of pure tochilinite penetrated by radial crack networks. Most lithologies typically consist of an abundant matrix of Mg-rich phyllosilicates, few or no surviving metal grains, and chondrules where >50 % of the primary anhydrous silicates have been replaced by phyllosilicates and/or carbonates. These features are all consistent with petrologic subtypes of CM2.0 – 2.4. However, the dominant lithology in section P30541 is less altered, with largely unaltered chondrule silicates, abundant Fe-Ni metal in chondrules and matrix, sulfides consisting of pyrrhotite with pentlandite rims, and a high abundance of T0 calcites (Fig. S11c). Its mineralogy is consistent with petrologic subtype of CM2.6.

12. Transmission Electron Microscopy

TEM observations show that phyllosilicates are the main constituents of the matrix and FGRs. Both S-bearing and S-poor phyllosilicates are present; the latter with d_{001} spacings of ~0.70 – 0.74 nm, and the former with d_{001} spacings of ~0.62 – 0.70 nm. Lattice spacings with repeating

units of two layers, consistent with 1:1 layered T-O phyllosilicates, are characteristic of serpentine-group minerals, as are the measured Mg-Fe silicate chemical compositions.

Crystals display a wide range of morphologies that are typical of CM carbonaceous chondrites (e.g., *97, 98*), including tubular chrysotile (Fig. S15 (a) and (b)) and platy cronstedtite whose SAED patterns indicate characteristic stacking disorder (Fig. S15 (c) and (d)). Fibers of tochilinite are also abundant in some of the Winchcombe meteorite lithologies. The ~1.8 nm d-spacing of these crystals, together with high-resolution images, show that they are comprised of coherently interstratified intergrowths of tochilinite (d_{001} = 10.8 nm) with serpentine (d_{001} = ~7.3 nm) (*97*). The FGRs contain phyllosilicate crystals of widely different sizes, within which are organic nano-globules that have been partially replaced by the phyllosilicates (Fig. 6 (b)).

13. Bulk Magnetic Properties

Figs. S16 (a) and (b) show the hysteresis loops for chips BM.2022,M1-95 and BM.2022,M3-32. Saturation magnetization (M_S), remanence magnetization (M_{RS}), coercivity (H_C), coercivity of remanence (H_{CR}), mass specific magnetic susceptibility (χ), and the S300 ratios of the measured Winchcombe meteorite are given in Table S16. The mass normalized M_S and M_{RS} values, and the H_C, H_{CR}, and mass specific magnetic susceptibility (χ) (provided here as log(χ)) values of the Winchcombe meteorite fall into the lower range of values reported for CM chondrites (*56, 99, 100*). The S300 ratios of chips BM.2022,M1-95 and BM.2022,M3-32 fall into the higher range exhibited by the CM chondrites, indicating higher abundances of magnetite relative to magnetic pyrrhotite (*100*).

Figs. S16 (c) and (d) show FORC diagrams of chips BM.2022,M1-95 and BM.2022,M3-32. Both FORC diagrams show similar characteristics, including a prominent central ridge that extends to ~0.1 – 0.15 T, characteristic of <0.1 μm single domain (SD) magnetic grains (*101*) and similar to previous analysis of CM chondrites (*56*). Chip BM.2022,M1-95 displays a more

extensive, symmetrical vertical spreading cantered near the origin, which indicates the presence of interacting vortex (Int-V) and/or larger, multi domain (MD) grains (*102*). A similar signal is observed in carbonaceous chondrites that contain magnetite framboids (clustered and magnetically interacting, 0.1 – 5 μm grains of magnetite), such as the CI chondrites, and the $C2_{ung}$ chondrites Tagish Lake and WIS 91600 (*56, 103, 104*).

Fig. S16 (e) shows PCA of the Winchcombe meteorite FORC diagrams alongside CI and CM chondrites with petrologic grades of 1.0 – 1.3 on the alteration scale of (*95*). The previously measured CI and CM chondrite FORC diagrams define endmembers in a region of PCA space within which most of the highly aqueously altered samples plot. The CM chondrites define a linear trend between two endmembers (smaller, <0.1 μm, SD magnetic grains, and slightly larger, 0.1 – 5 μm, V state magnetic grains), with the CI chondrites defining a third endmember (corresponding to closely packed, interacting magnetic assemblages, i.e., framboids and plaquettes). Both analyzed Winchcombe meteorite chips plot within the identified region enclosed by the end members, although notably closer to the Int-V/MD endmember defined by the CI chondrites rather than most other CM1.0 – 1.3 chondrites. This suggests the presence of more framboid and plaquette magnetite in the Winchcombe meteorite compared to other CM chondrites.

14. Computed Tomography

XCT imaging of the chips highlighted the diversity of lithologies in the Winchcombe meteorite. In total, 15 of the fragments were analyzed for evidence of petrofabrics; eight contained lithologies possessing weak-moderate, chondrule defined petrofabrics. All of the observed petrofabrics were characterized by long shape axis orientations plotting along a great circle girdle and short shape axis orientations clustering, a pattern indicative of foliation. Within three fragments (BM.2022,M1-84, 0.36 g; BM.2022,M2-34; BM.2022,M4-34, <0.01 g), multiple lithologies were distinguished by a difference in X-ray attenuation. In sample BM.2022,M2-34

three distinct lithologies were identified, two of which exhibited petrofabrics orientated in different directions (Fig. S17). In addition to chondrule defined petrofabrics, one fragment (BM.2022,M1-84) was characterized by a fracture defined fabric (Fig. S17). An average fracture trend of 156.1°relative to the top of the XCT slices was observed.

Macro-scale porosity extracted from four sub-volumes within BM.2022,M2-34 ranged from 0.56 – 4.21 %. Three sub-volumes were observed to contain cross-cutting fractures, producing porosity values >1.5 %. Sub-volume four was not observed to have cross-cutting fractures and consequently recorded a reduced porosity of 0.56 %. Within the sub-volume extracted from BM.2022,M3-31, a small cross-cutting fracture was observed, which was reflected in a porosity value of 0.99 %.

15. Thermogravimetric Analysis

Table S17 summarizes the mass loss in each temperature region for the Winchcombe meteorite. The total mass loss during heating from 15 – 1000°C was ~15 wt.%. The Winchcombe meteorite showed a mass loss at <100°C from terrestrial adsorbed water of 2.4 wt.%, similar to other CM chondrite falls and finds (Fig. S18). In contrast, the Winchcombe meteorite mass loss between 100 – 200°C was only 0.6 wt.% and lower than all other analyzed CM chondrites, except for a few highly altered hot desert finds. For CM chondrites, the main cause of mass loss in this temperature region is the breakdown of terrestrially formed sulphates, which is usually observed as a peak in the derivative curve at ~120°C. However, this peak was not seen for the Winchcombe meteorite, indicating low terrestrial contamination and modification.

Assuming all mass loss from 200 – 770°C was due to the dehydration and dehydroxylation of Fe-(oxy)hydroxides and phyllosilicates, the water abundance of the Winchcombe meteorite was calculated as 11.2 wt.%. This agrees with values of Winchcombe samples analyzed using stepped pyrolysis (Section 16) and is consistent with other highly altered CM chondrites (*83*).

16. Hydrogen Pyrolysis

Table S18 summarizes the data and Fig. S19 shows the abundance and isotopic composition of hydrogen released during the stepped pyrolysis. The bulk water content of the Winchcombe meteorite chips was calculated by excluding the releases at <200°C due to possible terrestrial modification. This resulted in water abundances of 9.3 wt.% for BM.2022,M2-39-a, 10.7 wt.% for BM.2022,M2-39-b and 11.4 wt.% for BM.2022,M2-39-c, giving an average for the Winchcombe meteorite of 10.5 ± 1.1 wt.%, in good agreement with the estimate from the TGA (Table S17). Excluding the low temperature steps yielded bulk δD values of −145.8 ‰ for BM.2022,M2-39-a, −138.6 ‰ for BM.2022,M2-39-b, and −140.2 ‰ for BM.2022,M2-39-c, resulting in an average for the Winchcombe meteorite of −142 ± 4 ‰.

17. Carbon and Nitrogen Pyrolysis

Carbon and nitrogen data from stepped combustion of samples BM.2022,M1-85 and BM.2022,M1-86 are summarized in Figs. S20 and S21 and Tables S19 and S20. The carbon abundance and isotopic composition are typical of CM chondrites (*23, 105*). The two samples exhibited very similar behavior on combustion, although there are subtle differences that illustrate the heterogenous nature of the Winchcombe meteorite.

The bulk of the carbon occurs as organic matter, combusting below 500°C. Variation in isotopic composition within this temperature range indicates that at least three different organic components are present, with $\delta^{13}C$ between −20 ‰ and +15 ‰. The material released on combustion between room temperature and 100 °C has a $\delta^{13}C$ around 0 ‰ and may correspond with the species identified by selected ion flow tube-mass spectrometry (SIFT-MS) (Section 18). The isotopically lighter material combusting between 350 – 500 °C is likely to be the abundant macromolecular material known to occur in CM chondrites (*106*), almost certainly mixed with CO_2 from nanodiamonds (*107*). A second maximum in carbon yield carbon occurs at 600 °C with

$\delta^{13}C$ between +40 ‰ and +60‰; comparison with other CMs suggests that this is carbonate, probably calcite (*108*). At least one of the components has $\delta^{13}C$ of at least +150 ‰, probably from a mixture of presolar graphite and SiC (e.g., *109*).

Like carbon, the abundance and isotopic composition of nitrogen in the Winchcombe meteorite are typical of CM chondrites (*23, 105*), with both samples exhibiting similar behavior on combustion. The combustion profiles are dominated by release of nitrogen from organic matter: there is a maximum at 250 – 300 °C, which accounts for ~10 % of the total nitrogen, with $\delta^{15}N$ around +50 ‰. This component is unresolved in carbon data, but the nitrogen isotopic composition is characteristic of meteoritic organic acids (*110*). The bulk of the nitrogen, though, like the carbon is from combustion of macromolecular material, depleted in both ^{15}N and ^{13}C relative to the less refractory organics (*111*). The sharp and pronounced drop in $\delta^{15}N$ at 400°C is a sign that nanodiamonds are co-combusting with the organic material. Above 600 °C, we see separate presolar components enriched and depleted in ^{15}N – also evidence of presolar graphite and SiC (*109*).

17.1 Noble Gases

Table S21 gives the total concentration (in cm^3 STP g^{-1}) of ^4He, ^{20}Ne, ^{36}Ar, and ^{132}Xe in the Winchcombe meteorite samples BM.2022,M1-85 and BM.2022,M1-86. The concentrations are generally an order of magnitude higher than observed in typical CM meteorites (e.g., (*15*)), where planetary (or Q-type) noble gases dominate. The Ne isotopic composition of the individual temperature steps mostly plot on the mass fractionation line (MFL) indicating the presence of fractionated solar wind (SW) (Fig. S22), implying that the meteorite is from the regolith of its parent body where it was irradiated by SW particles. However, since the MFL is indistinguishable from the SW-Q mixing line, a contribution from Q cannot be ruled out. Its presence is clearly visible in sample BM.2022,M1-85, which has a lower Ne content than BM.2022,M1-86. In the

latter case, some data points plot above SW composition indicating higher contribution of the (fractionated) SW component.

Fig. S22 shows that some data points fall of the SW-Q mixing line, lying within the SW-Q-COSM triangle, suggesting the presence of cosmogenic Ne. This is more pronounced for BM.2022,M1-85, which has a lower overall concentration of Ne. The calculated concentration of cosmogenic ^{21}Ne in 1a-85 is $(1.6 \pm 0.8) \times 10^{-9}$ cm^3 STP g^{-1}, which corresponds to a ^{21}Ne CRE age of 0.55 (± 0.3) Ma (assuming a $^{21}Ne_{cosm}$ production rate of 0.288×10^{-8} cm^3 g^{-1} yr^{-1} established for CM meteorites by (*112*)). This age is slightly longer than those measured in samples BM.2022,M2-36 and BM.2022,M4-7 (Sections 4 and 5) but still close to the main cluster of exposure ages for CM meteorites (*15*).

18. Selected Ion Flow Tube-Mass Spectrometry

Fig. S23 shows that no significant differences were found between the samples and there was a general decrease in abundance with increasing carbon number. Aldehydes and ketones were found to be the most abundant species present, followed by alcohols and then carboxylic acids. This profile is consistent with previous reports of ultraviolet (UV) emissions from the CM chondrite Murchison and analysis of volatiles by proton-transfer reaction mass spectrometry (PTR-MS) (*113*), but significantly different from the results of (*114*), who concluded that by solvent extraction, carboxylic acids are the most abundant free compounds in Murchison and dominate the free organic inventory. The low level of carboxylic acids determined by both the thermal and UV method is likely due to the carboxylic acids being present in their salt form, thus thermally stable and non-volatile.

19. Low Voltage SEM-EDS

Many fragments were found to be coated in micrometer to sub-micrometer sized particles with the same composition as the bulk meteorite fragments, suggesting that they are highly

electrostatic in nature. The fragments were composed mainly of silicate minerals, with carbonate, phosphate, and sulfide minerals also present throughout. Despite mapping the fragments over several days, there was no evidence for phases such as halite or other salts, elemental sulfur or oldhamite. However, carbon- and nitrogen-rich areas were observed heterogeneously distributed within the fragments. High resolution imaging revealed the regions (typically ~10's μm in size) to be carbonaceous, likely organic materials, often with "globule-like" morphologies (Fig. S24). Based on their textural settings (i.e., clearly within the meteorite matrix), and also the rapid recovery and minimal handling of the fragments prior to analysis, the carbonaceous materials are interpreted as being indigenous to the Winchcombe meteorite. Furthermore, in some instances, they are intimately associated with minerals, such as carbonates, that are expected to have formed from extraterrestrial fluids on the asteroid parent body.

20. Liquid Chromatography-Mass Spectrometry

PCA of untargeted LC-MS data indicated that the solvent extracts from both meteorite chips contained many organic molecules in common with each other, but not present in the environmental samples (Fig. S26). This suggests that despite the detection of a number of likely contaminants (molecules found in the soil sample extracts, as well as the meteorite extracts), a significant amount of indigenous extraterrestrial organic matter remained in the meteorite chips.

Fig. S26 shows that the six Winchcombe meteorite extracts cluster closely together, whilst the environmental samples cluster away from both the meteorite extracts and each other. The first principal component shown on Fig. S26 is responsible for 75.1 % of the variance in the distribution of the organic molecules in the extracts, leading to the separation of the Winchcombe meteorite extracts from the environmental samples. This close clustering of the Winchcombe extracts, and the relatively high variance which PC1 accounts for, further suggests that there was minimal contamination, and much of the indigenous organic material remained in the meteorite.

A large number (>200) of organic molecules were detected at high intensities in the Winchcombe meteorite extracts from both Site 1 and Site 6 but were below the detection limits in the environmental samples. Approximately 10% of these were identified as organic sulfonate compounds, with several alkyl sulfonate of various chain lengths (ethanesulfonate, propanesulfonate, pentanesulfonate, and hexanesulfonate). Organic sulfonates have previously been detected in the Murchison CM2 chondrite (*115*).

21. Gas Chromatography-Mass Spectrometry

The pristine nature of the Winchcombe meteorite is reflected by its amino acid content (Table S23). In the hot water extracts of the Winchcombe meteorite, trifluoroacetyl (TFA)-derivatives of two up to six carbons (C_2 – C_6) amino acids were identified and quantified. The total (free + bound peptide-like) amino acid abundance in the 6M HCl hydrolyzed hot water extract of the Winchcombe meteorite was 1132 ± 49 ppb (Table S23), which is lower than most primitive CM chondrites such as Murchison (14,600 ppb) (*116*). The presence of terrestrially rare amino acids (e.g. α-aminoisobutyric acid (α-AIB), α-, β-, and γ-amino-n-butyric acids (ABA), isovaline), and the elevated abundance of some of these compounds, such as α-AIB (467 ± 17 ppb) and isovaline (391 ± 17 ppb) – the two most abundant amino acids in the Winchcombe meteorite – strongly indicate that these amino acids are extraterrestrial in origin. Terrestrial biology uses only the L-enantiomers of chiral amino acids except in rare scenarios. Therefore, the indigenous nature of the detected amino acids in the Winchcombe meteorite is unequivocally established by the racemic mixtures of the D- and L-enantiomers of both non-protein amino acids (e.g. $D/L_{isovaline} = 1.06 \pm 0.15$) and common protein amino acids (e.g. $D/L_{alanine} = 1.13 \pm 0.16$).

Protein amino acids that are derived from terrestrial contamination, such as serine and threonine, were found predominantly as the L-enantiomers (up to enantiopure) in the soil collected from Site 1 (Table S4), which are absent in the Winchcombe meteorite. Biologically derived amino

acids often increase in abundance after acid hydrolysis as they are released from their bound form, as was observed in the Site 1 soil. This contrasts with what was observed for the Winchcombe meteorite, providing further compelling evidence against any significant contribution of the amino acids from a biological origin.

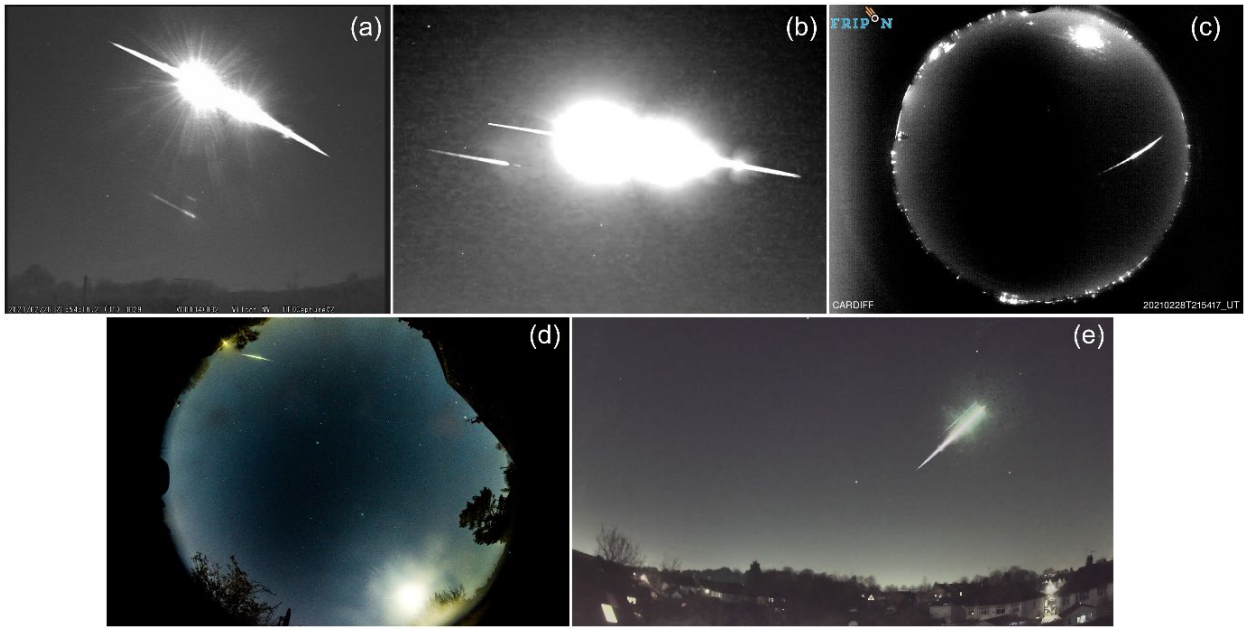

Figure S1. The Winchcombe fireball, as observed by the UKFAll camera networks. (a) UKMON camera in Wilcot; (b) GMN camera in Hullavington; (c) SCAMP/FRIPON camera in Cardiff; (d) UKFN camera in Welwyn; (e) AllSky7 camera in Nuneaton. A reflection in the optics that is parallel to the fireball is also visible in insets (a), (b) and (e).

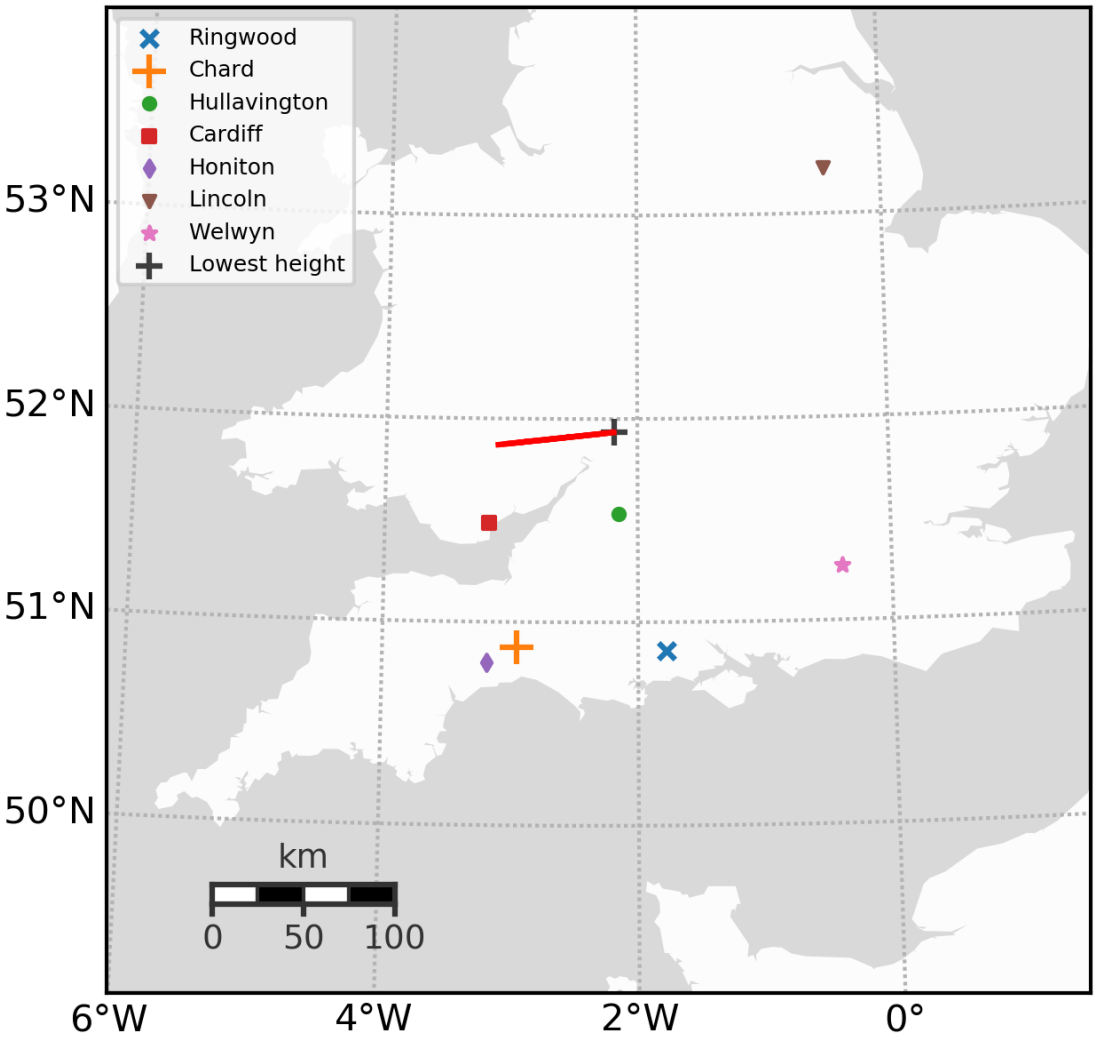

Figure S2. The Winchcombe fireball trajectory (red line) and locations of cameras used for astrometric measurements.

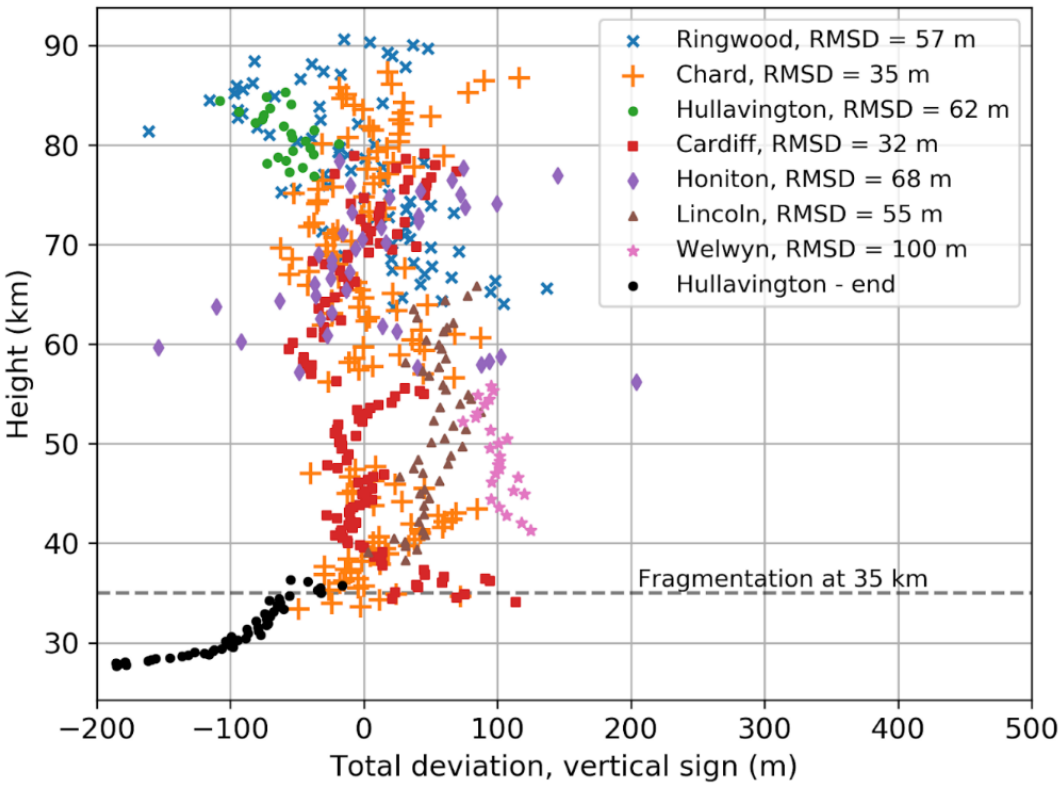

Figure S3. Trajectory fit residuals versus height. RMSD stands for root-mean-square deviation. The measurements from Hullavington were only done at the beginning and the end, as the fireball was too bright in the middle of the flight for accurate astrometric picks.

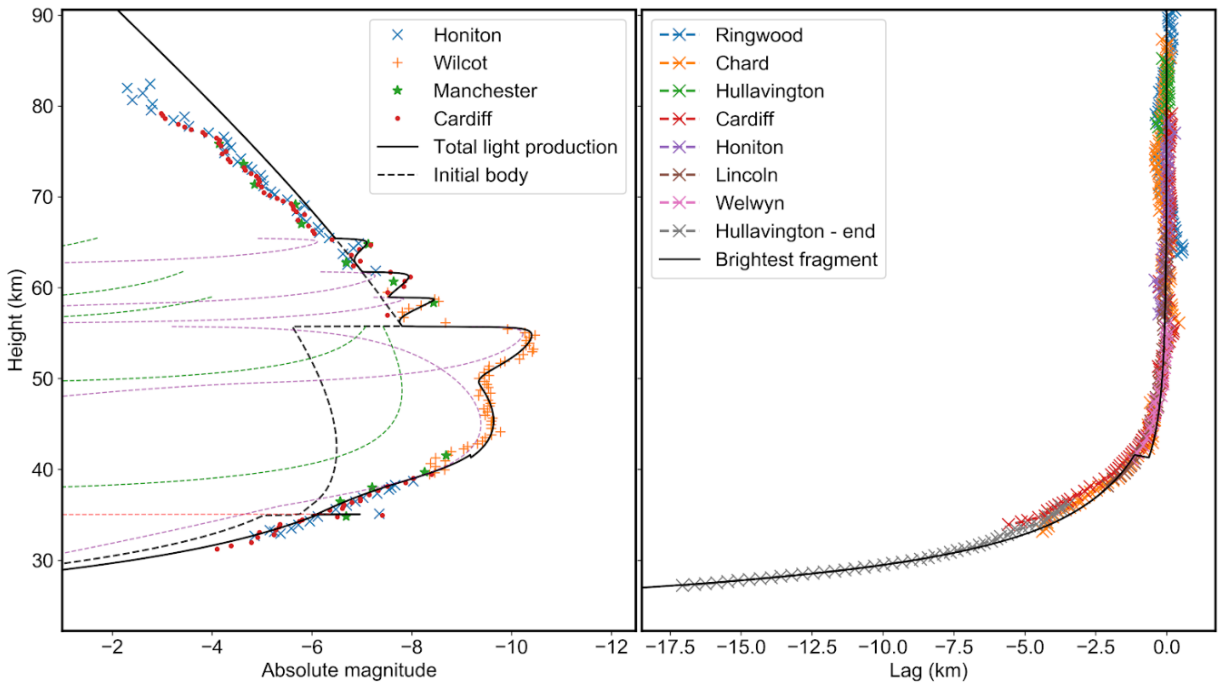

Figure S4. Fit of the ablation model (black line) to the observed light curve (left) and the deceleration (right) for the Winchcombe fireball. Contributions to the total light production of individual fragments is given in dashed lines; black for the magnitude of the main body, green for eroding fragments, purple for grains released by erosion, and orange for dust released directly from the main body.

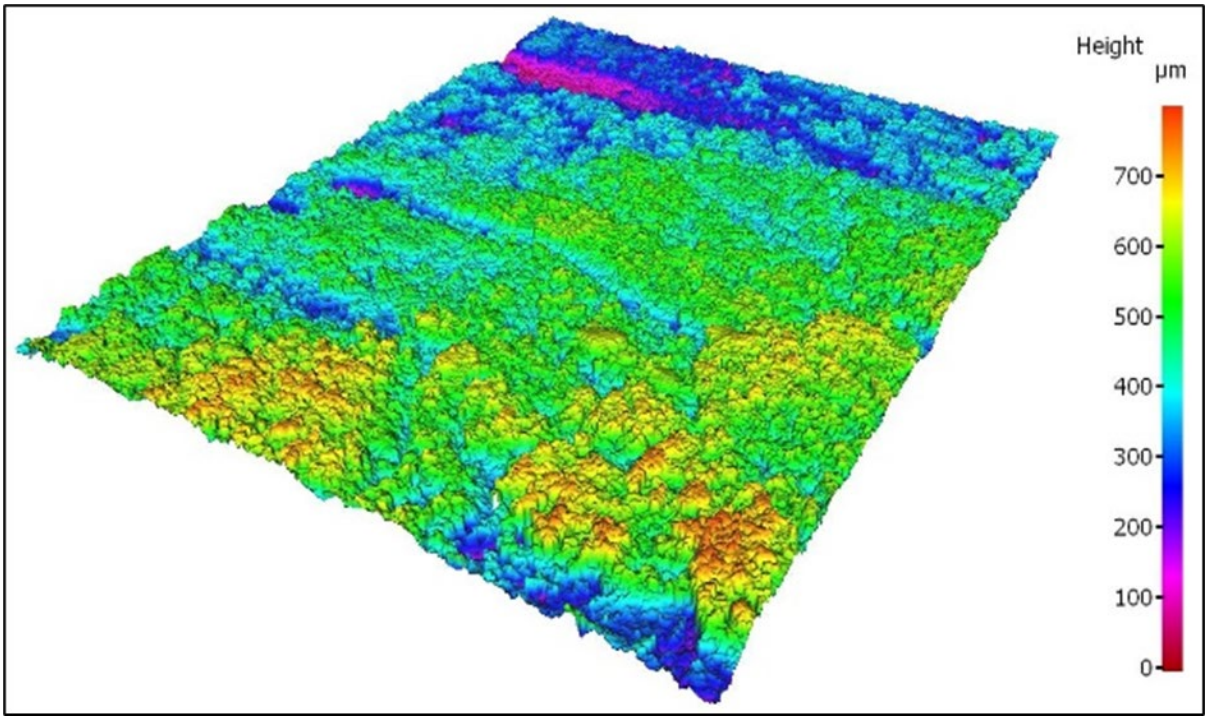

Figure S5. A 1 cm^2 surface profile of the Winchcombe meteorite sample used in the reflectance study, measured using an Alicona 3D® instrument. Lateral resolution = 10 µm; vertical resolution = 1 µm.

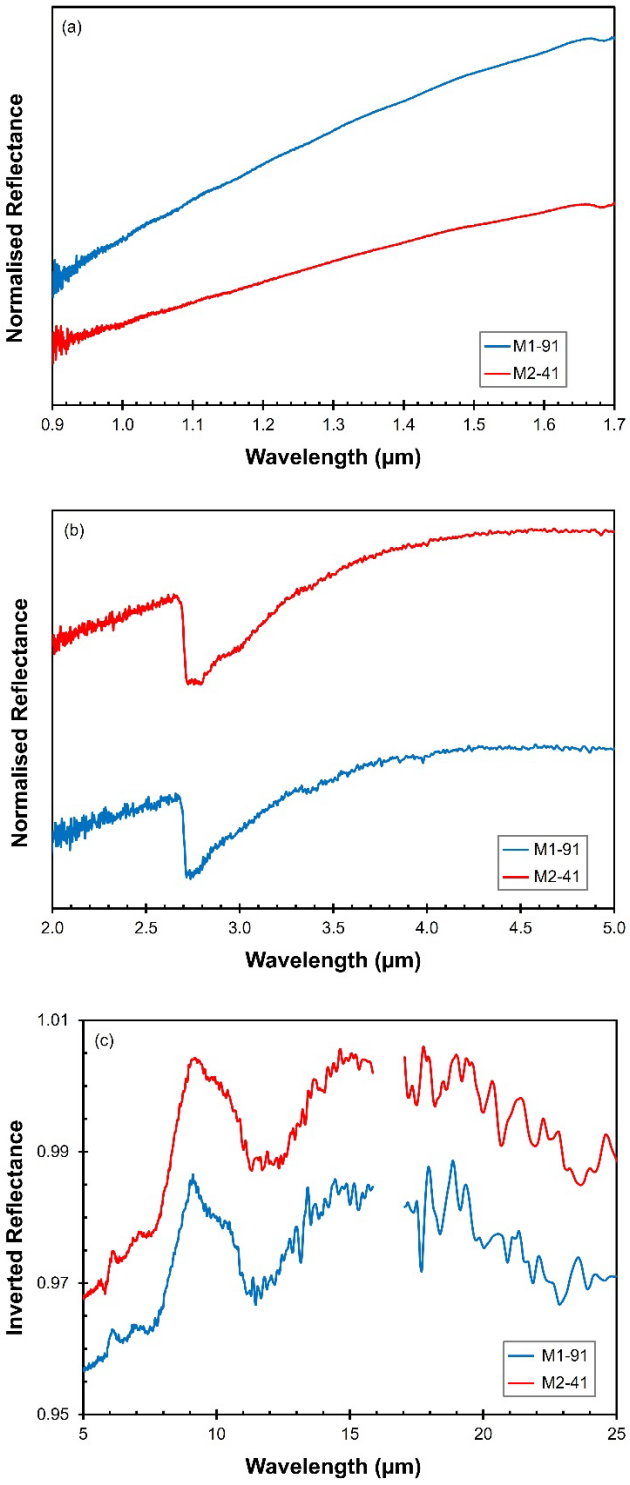

Figure S6. VNIR ((a) and (b)) and MIR (c) reflectance spectra for powdered Winchcombe meteorite samples BM.2022,M1-91 and BM.2022,M2-41. The slope in (a) is consistent with a fine particulate sample with a high phyllosilicate abundance. Features in (b) are related the water content and phyllosilicate composition, and features in (c) suggest small variations in the olivine content and degree of aqueous alteration recorded by the samples.

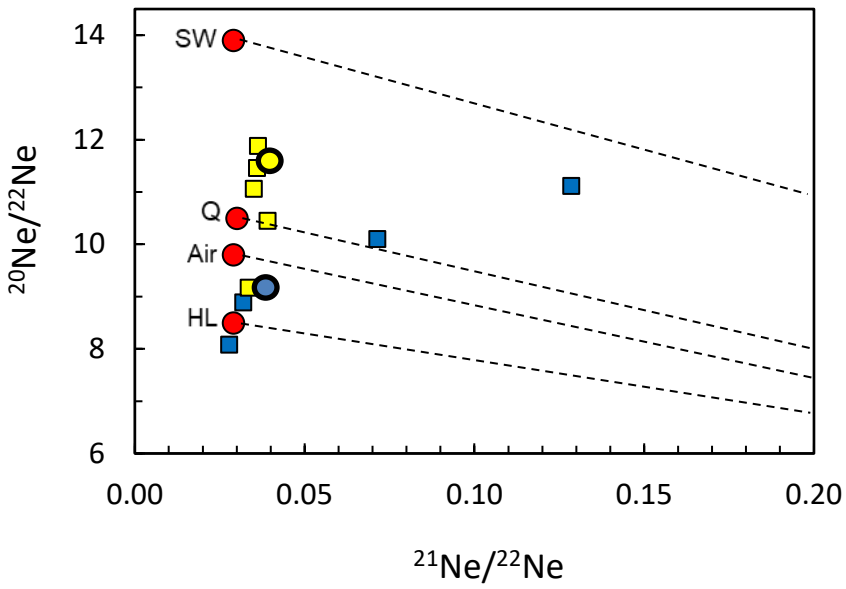

Figure S7. Neon isotope composition of gases released by step heating two samples of the Winchcombe meteorite (BM.2022,M2-36 and BM.2022,M4-7). The isotopic composition of the total gas from each sample is shown as circles. Black dashed lines represent mixing between the main trapped components (red circles: solar wind (SW; (*117*)), Air (*118*), Q (*84*), and HL (*85*)) with cosmogenic Ne derived from Galactic Cosmic Rays (*119*).

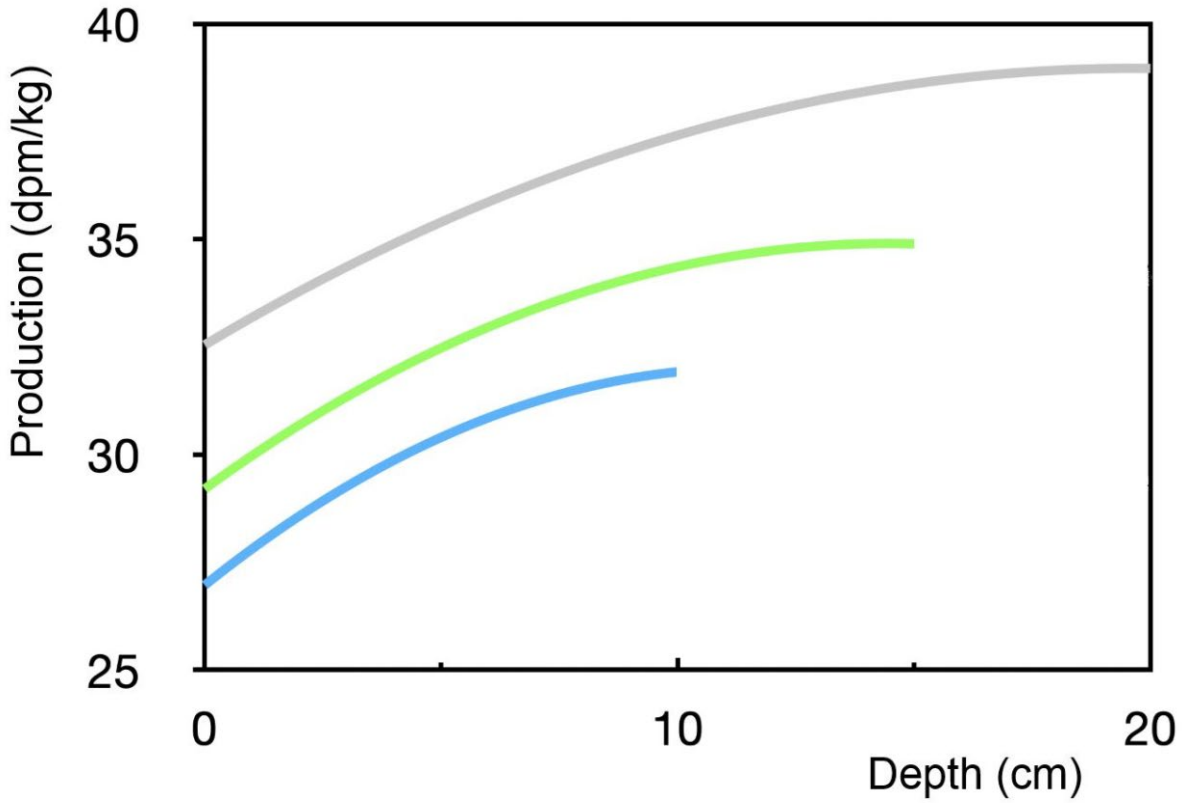

Figure S8. Saturated ^{26}Al production rates in the Winchcombe meteorite with radius of 10 and 20 cm, estimated from Monte Carlo simulations (adjusted for the meteorite chemical composition) (*39*).

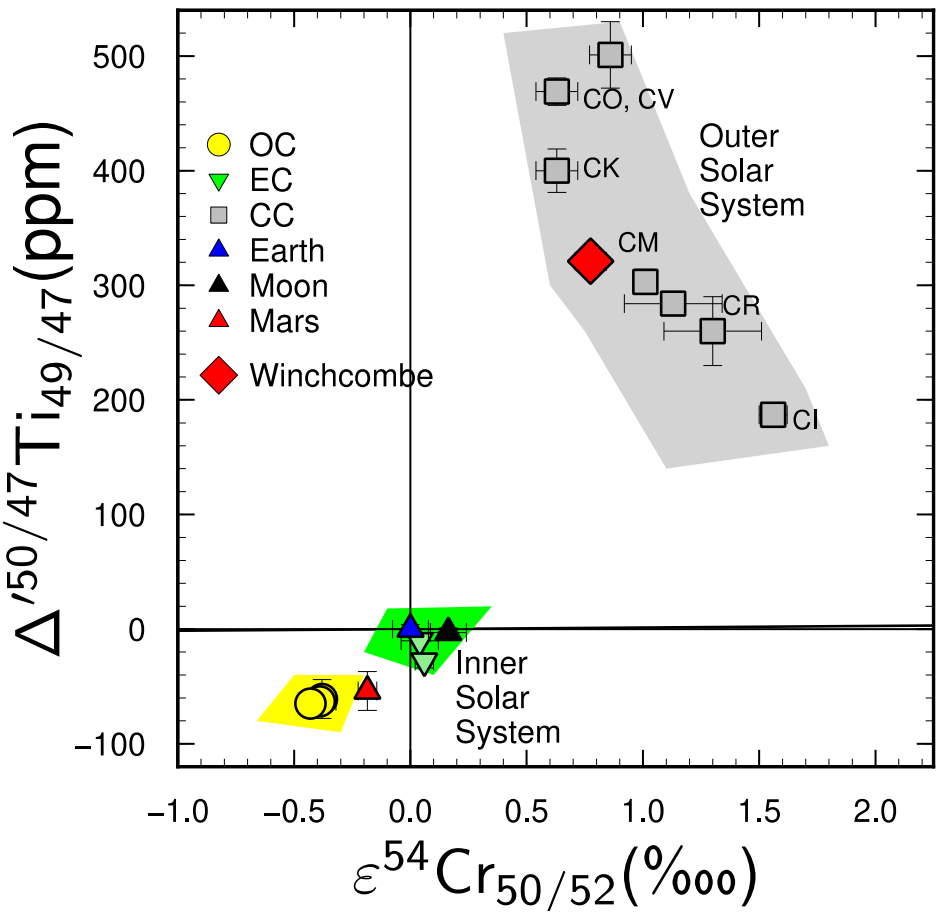

Figure S9. Plot showing the Cr and Ti isotope composition of the Winchcombe meteorite and various other meteorite groups (data from (*120*) and references therein). The isotope compositions of the Winchcombe meteorite plot with the other CM carbonaceous chondrites in the outer Solar System field. The $\varepsilon^{54}Cr_{50/52}$ are given in ‰ (parts per ten thousand) and $D'^{50/47}Ti_{49/47}$ are given in ppm (parts per million) and the analytical techniques are described elsewhere in the supplementary material. Points from OC and EC are group averages while CC are points for which the same meteorite was measured for both Cr and Ti.

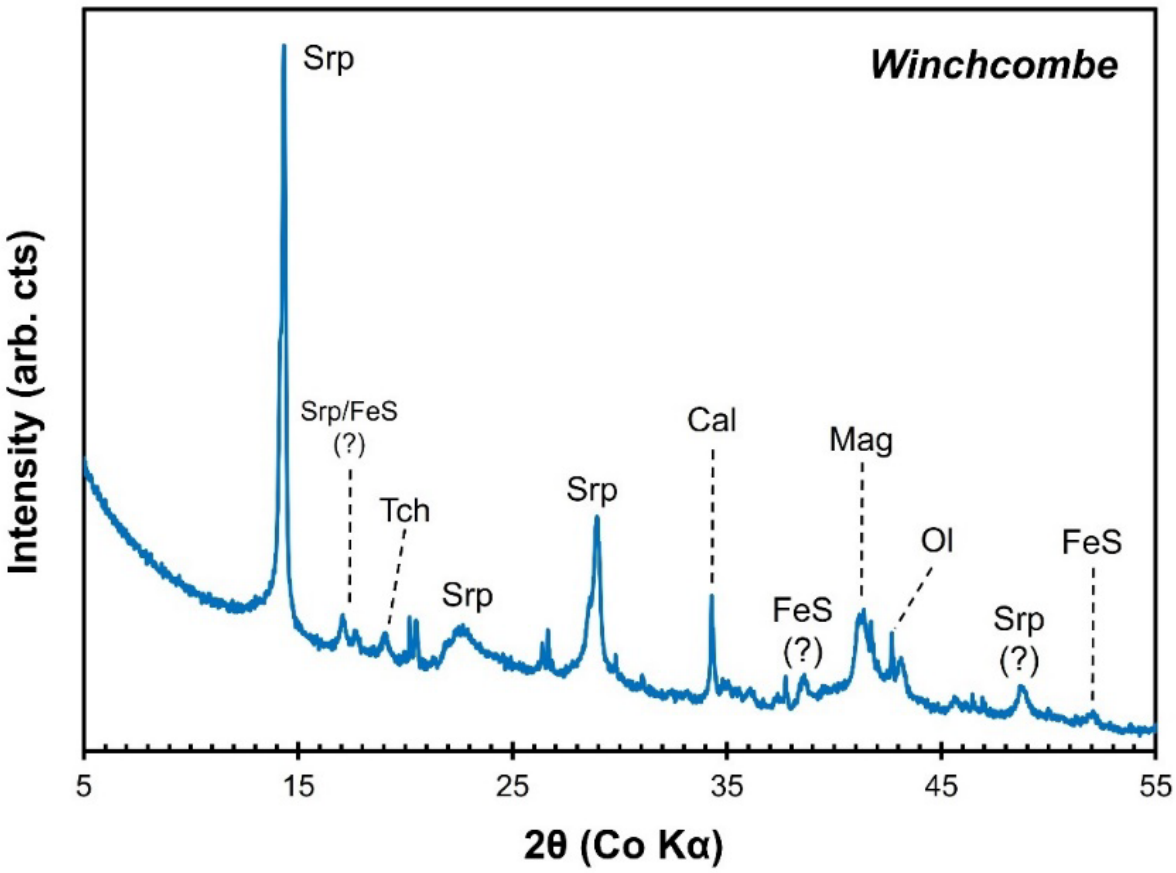

Figure S10. XRD pattern of Winchcombe meteorite sample BM.2022,M1-88 collected using a PANalytical X'Pert Pro scanning XRD. Minerals identified include phyllosilicates (serpentine (Srp)), tochilinite (Tch), calcite (Cal), Fe-sulfides (pyrrhotite (FeS), magnetite (Mag), and olivine (Ol).

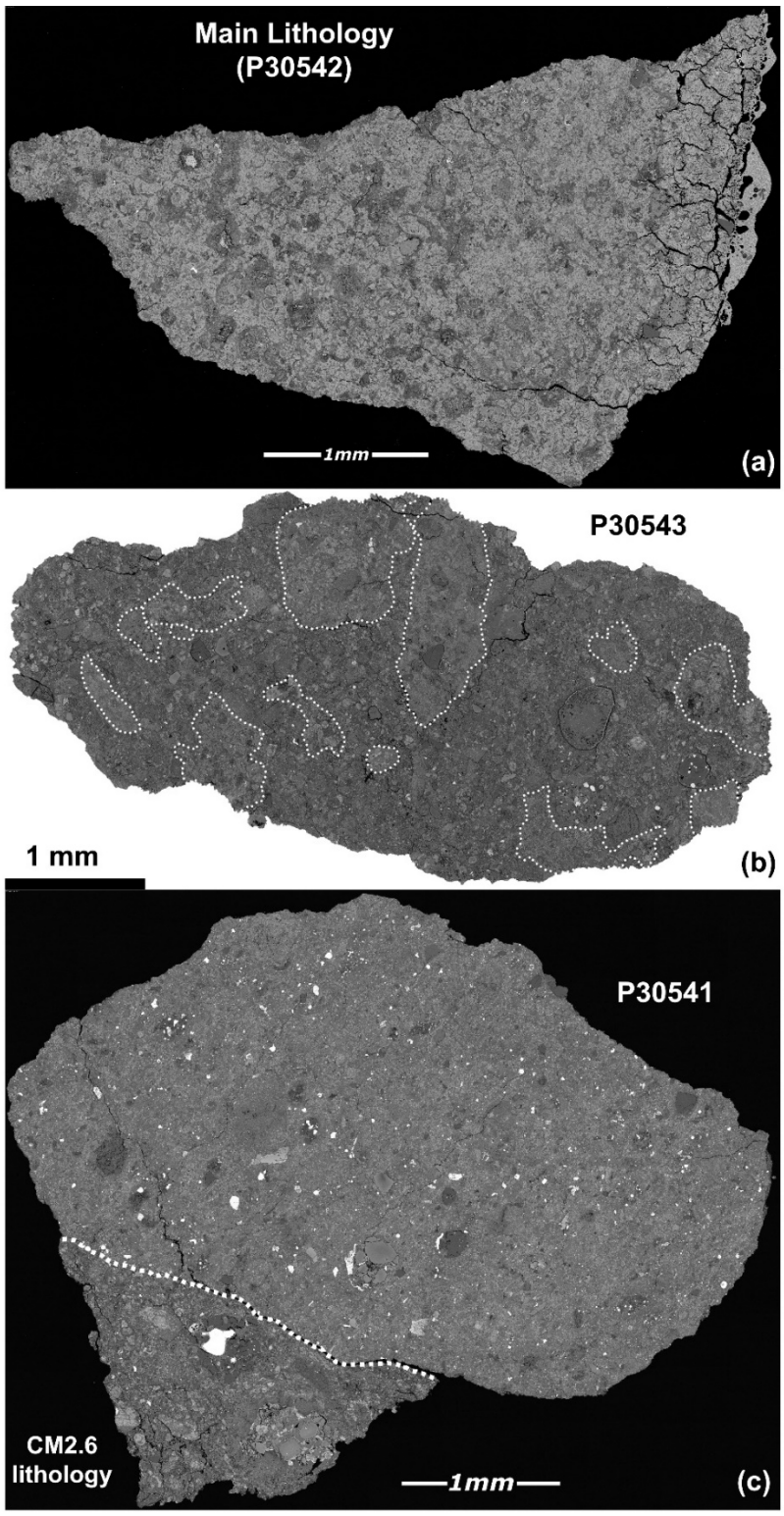

Figure S11. Example BSE overview images of Winchcombe meteorite samples. (a) P30542 only contains the main lithology identified in the Winchcombe meteorite, whereas (b) P30543 and (c) P30541 are comprised of multiple lithologies (highlighted by dashed white lines).

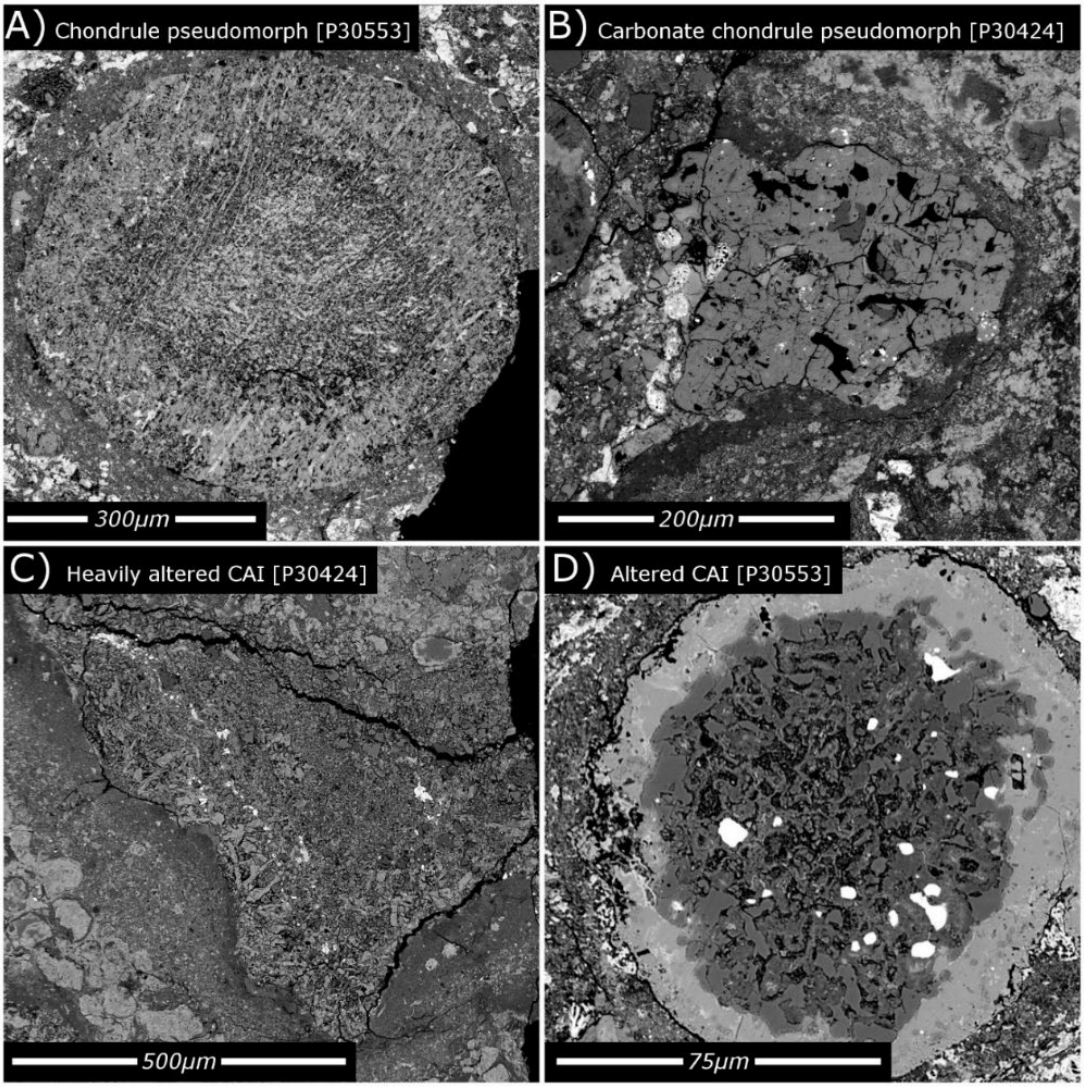

Figure S12. BSE images showing chondrule pseudomorphs with interiors replaced by (a) phyllosilicates and (b) carbonates, and examples of (c, d) altered CAIs in the main lithology of the Winchcombe meteorite.

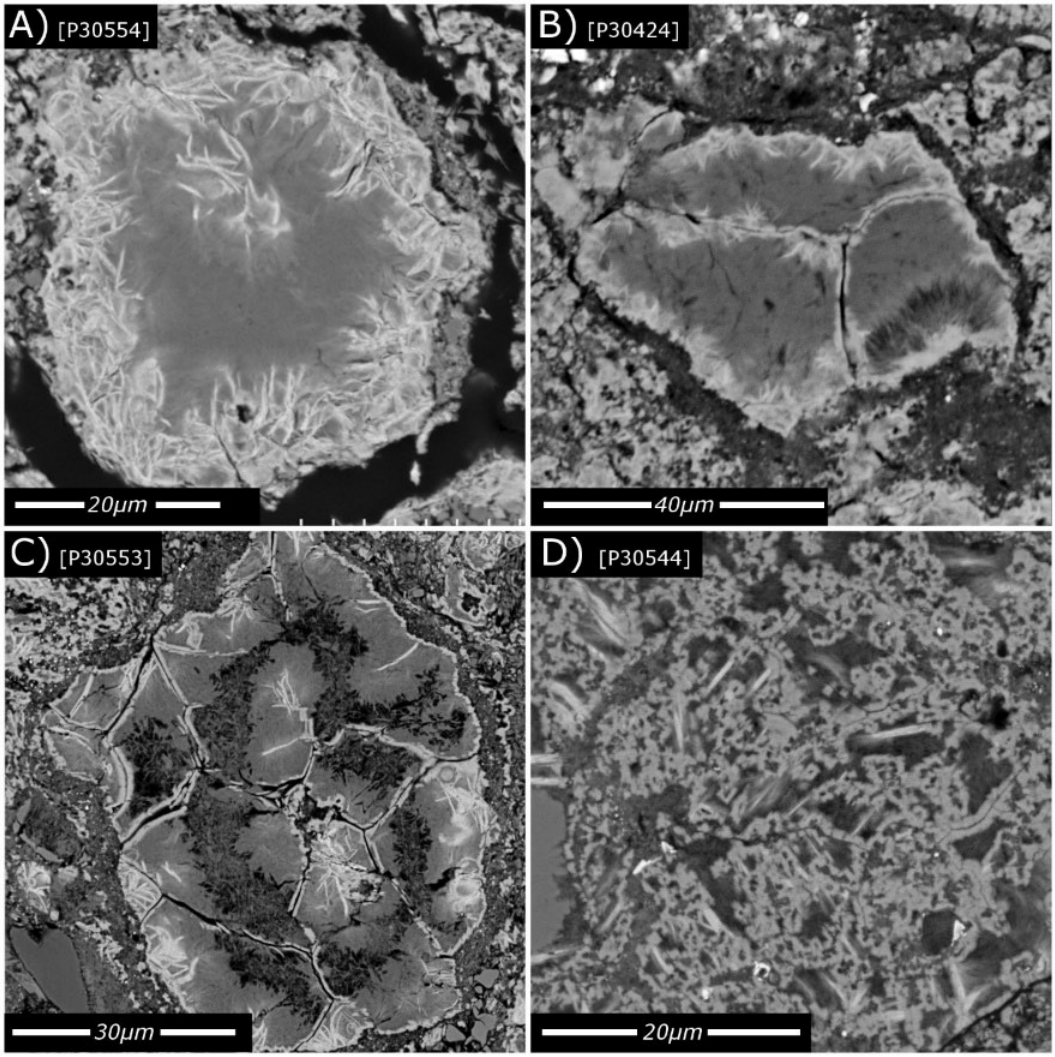

Figure S13. BSE images showing examples of coarse phyllosilicate clumps in the main lithology of the Winchcombe meteorite.

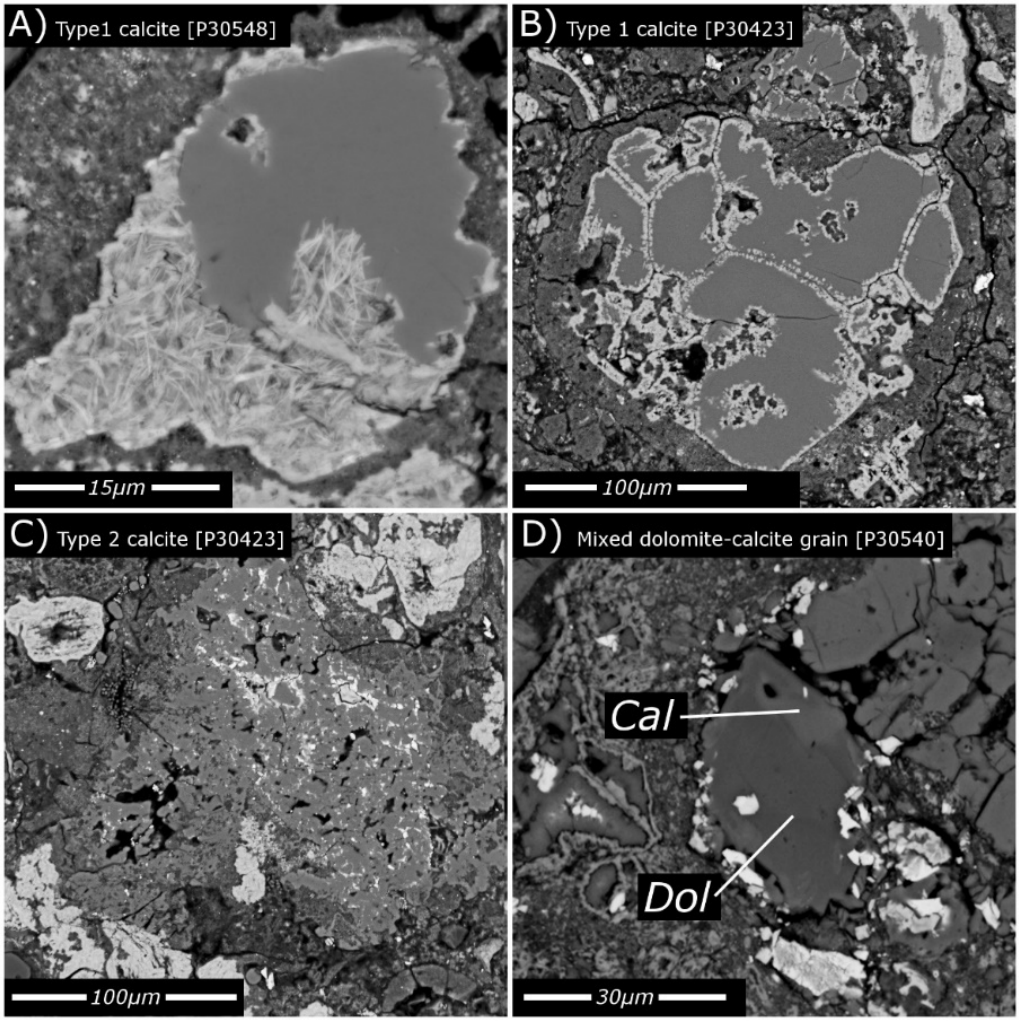

Figure S14. BSE images showing examples of (a, b) type 1 and (c) type 2 calcite, and (d) mixed calcite-dolomite in the minor lithologies of the Winchcombe meteorite.

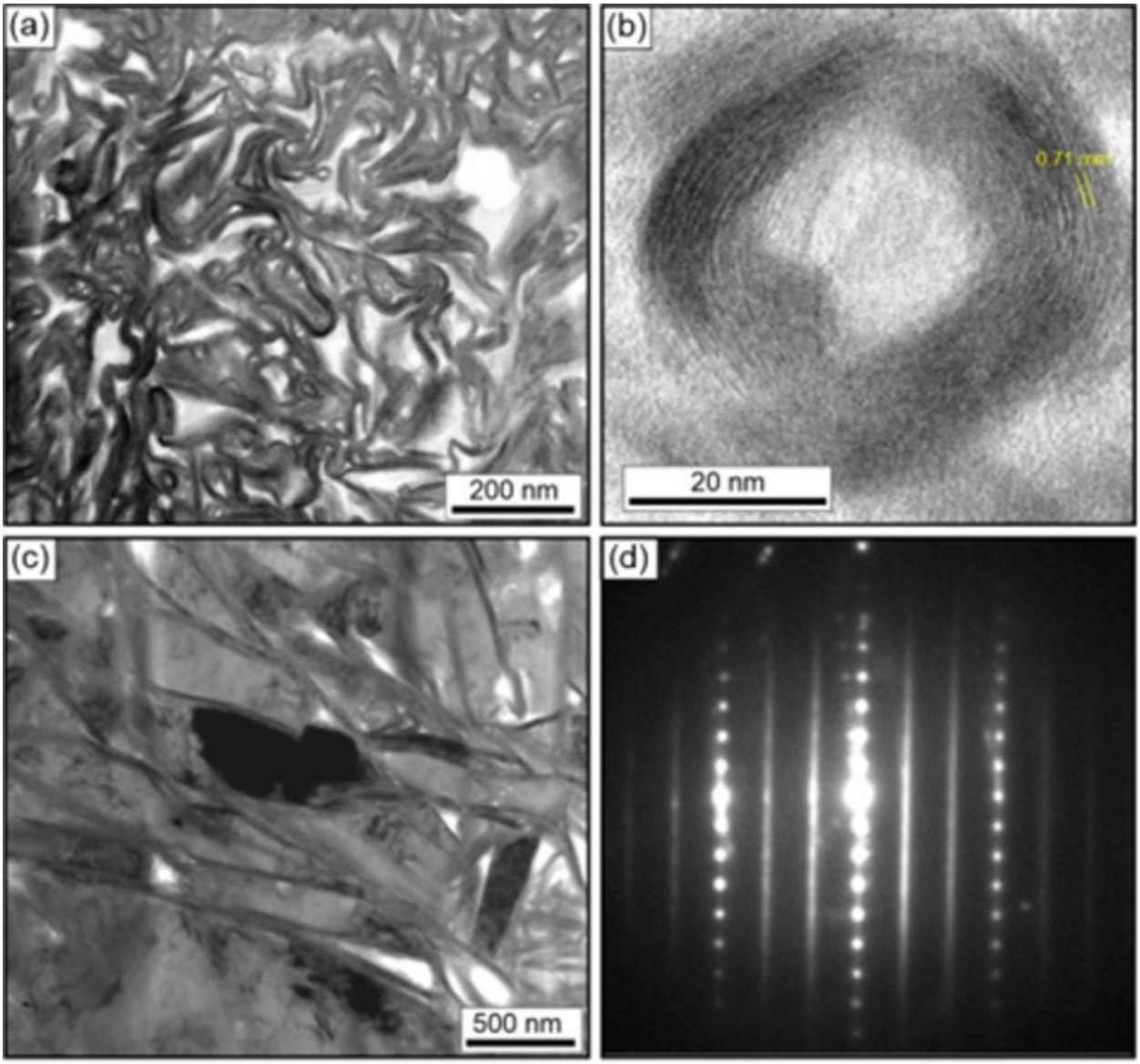

Figure S15. (a) Bright-field TEM image of an area of matrix that contains abundant curved and tubular chrysotile crystals. (b) High-resolution image of a chrysotile tube with a ~0.71 nm lattice spacing consistent with 1:1 layered T-O phyllosilicates such as serpentine and chrysotile. (c) Bright-field image of platy cronstedtite crystals. (d) SAED pattern of the crystal in the middle of (c). The spots have a d-spacing of 0.72 nm, and the streaking of the k≠3 rows is indicative of stacking disorder in the cronstedtite lattice.

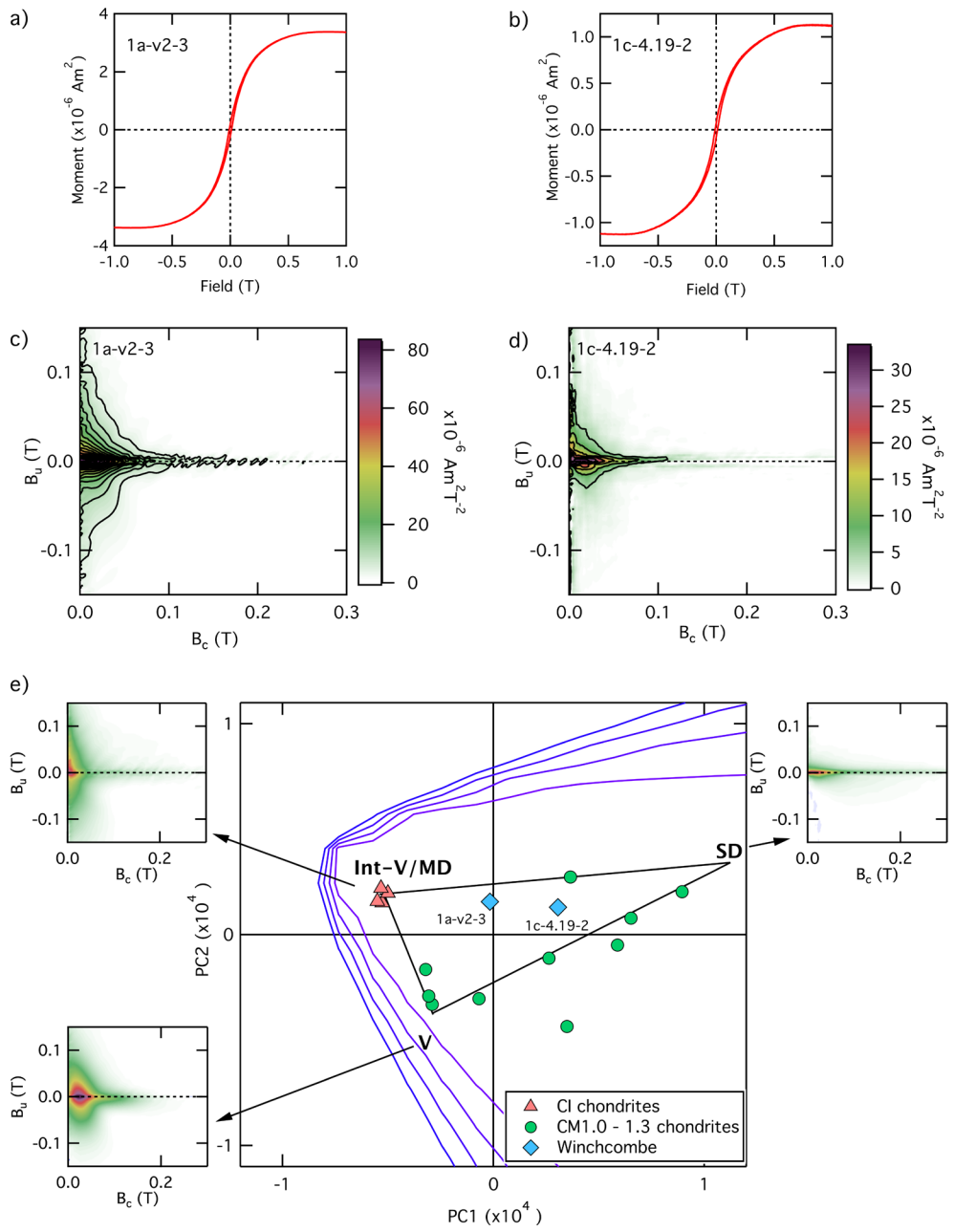

Figure S16. (a) Hysteresis loop of chip BM.2022,M1-95 (1a-v2-3 on figures); (b) Hysteresis loop of chip BM.2022,M3-32 (1c-4.19-2 on figures); (c) FORC diagram of chip BM.2022,M1-95; (d) FORC diagram of chip BM.2022,M3-32; and (e) Score plot displaying the proportions of PC1 and PC2 present in CI1.0 chondrites, CM1.0-1.3 chondrites, and Winchcombe meteorite chips BM.2022,M1-95 and BM.2022,M3-32. The Winchcombe meteorite data plot within the range of FORC diagrams defined by CI1.0 and CM1.0-1.3 chondrites, overlapping with the CM chondrites, but displaying a higher proportion of interacting vortex/multi-domain (Int-V/MD) particles. V = Vortex state, SD = Single Domain. Contours of feasibility metrics have been superimposed onto the score plot to help identify regions where physically realistic endmembers could be situated, with contours between 0.90 and 0.98 shown with intervals of 0.02. CI and CM chondrite data adapted from (*56*).

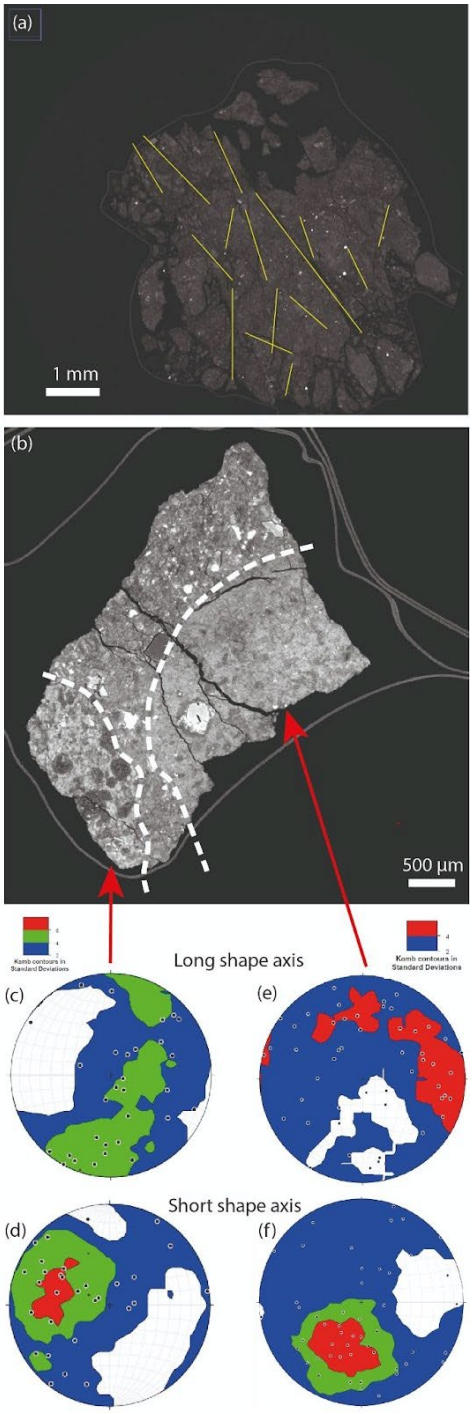

Figure S17. Example XCT data from Winchcombe meteorite samples BM.2022,M1-84 and BM.2022,M2-34. (a) and (b) – Example CT slice from two samples, with (a) showing aligned fractures and (b) showing three distinct lithologies distinguishable by their texture and contrast variations. (c) and (e) – lower hemisphere projection of the long shape axis of chondrules showing a weak-moderate girdle fabric. (d) and (f) – lower hemisphere projection of the short shape axis of chondrules showing a weak-moderate lineation fabric. There preferred alignments in the long and short shape axis of chondrules are consistent with a foliation fabric caused by compaction.

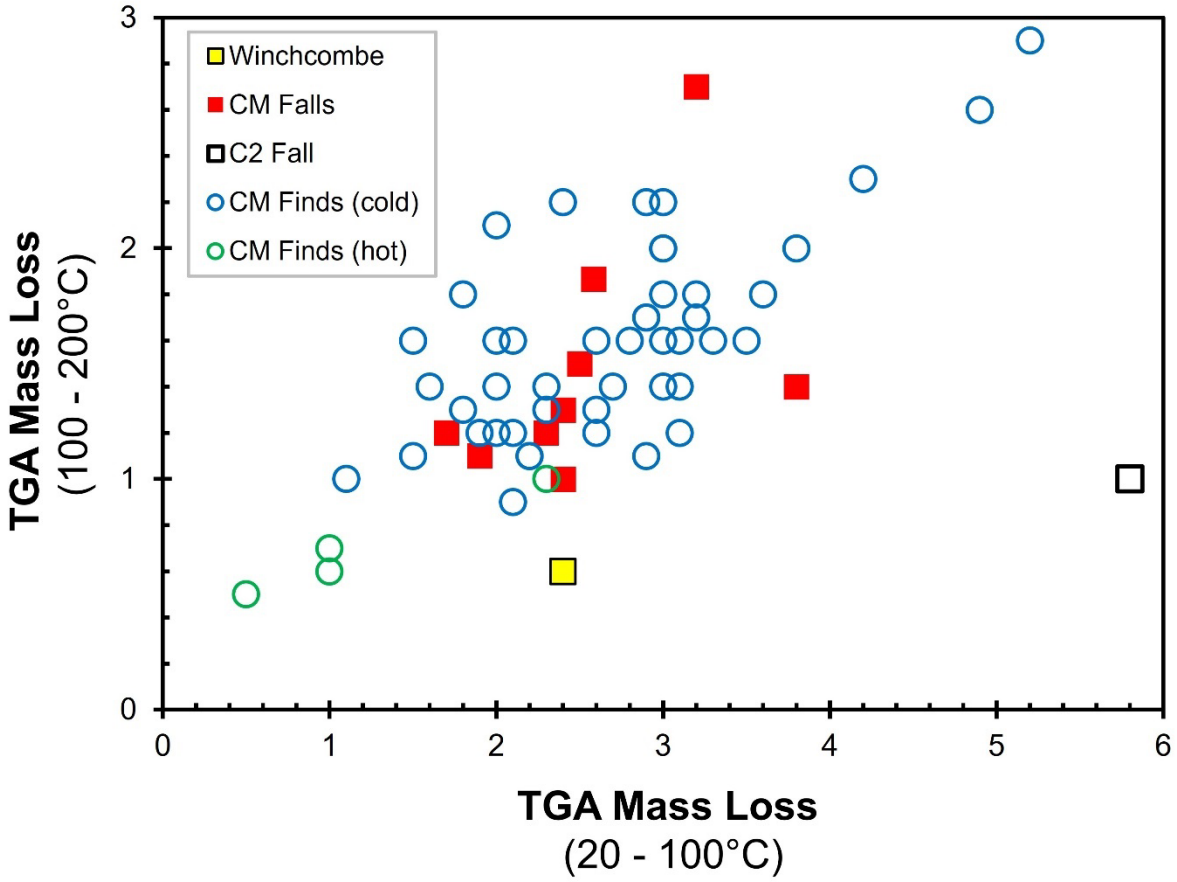

Figure S18. TGA mass loss between 20 – 100°C and 100 – 200°C for a sample of the Winchcombe meteorite analyzed on the 5th March 2021 compared to other CM/C2 chondrites measured in our laboratory. Data are from (*60*, *83*).

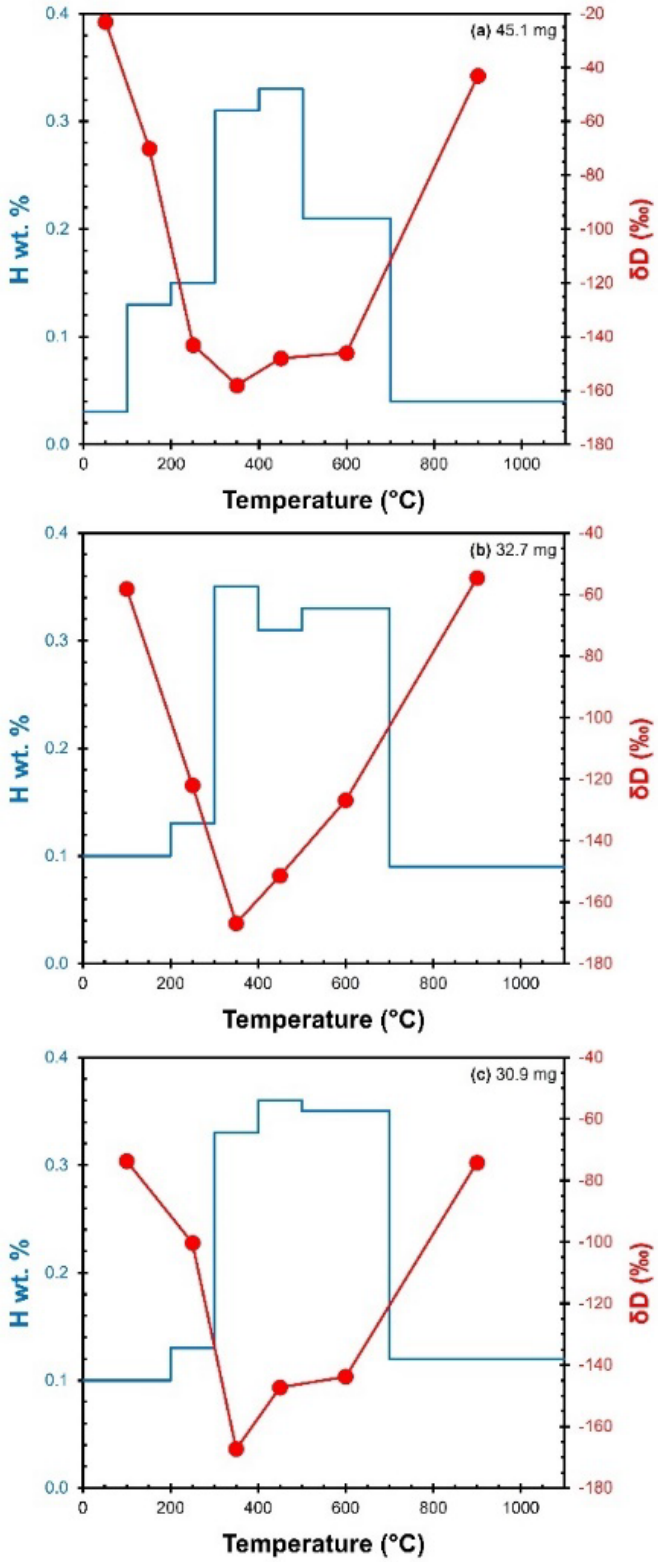

Figure S19. Abundance and isotopic composition of hydrogen released during stepped pyrolysis of the Winchcombe meteorite samples (a) BM.2022,M2-39-a, (b) BM.2022,M2-39-b, and (c) BM.2022,M2-39-c.

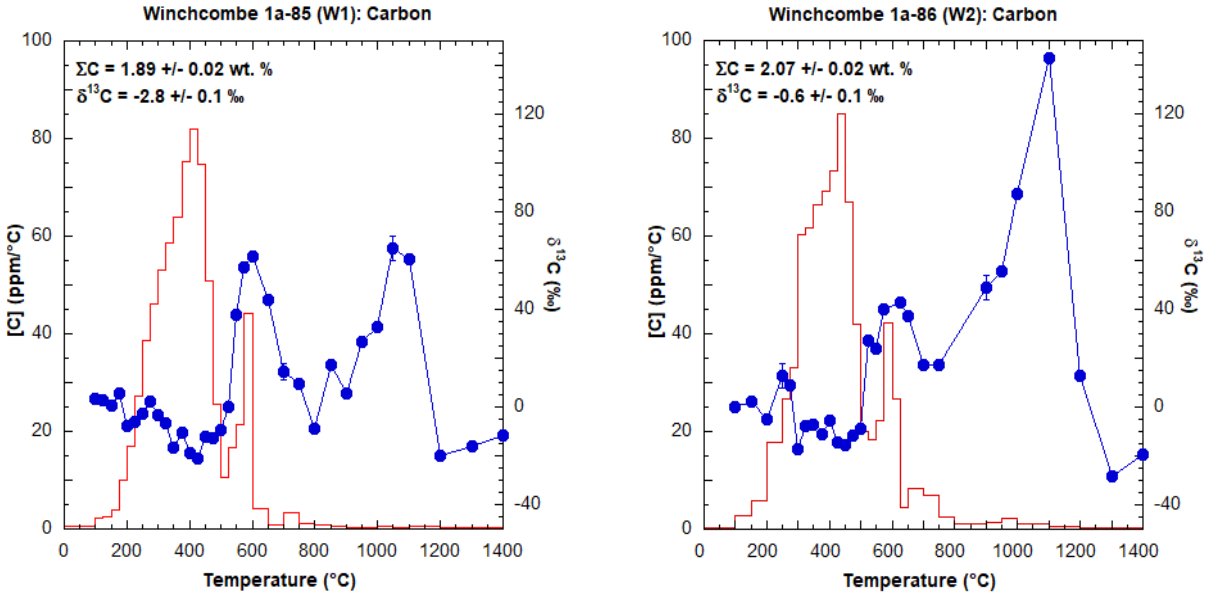

Figure S20. Carbon data from stepped combustion of Winchcombe chips BM.2022,M1-85 (5.0502 mg; 1a-85 (W1) on figure) and BM.2022,M1-86 (5.0981 mg; 1a-86 (W2) on figure). Abundance (in ppm $°C^{-1}$; scaled on the left axis) is the red histogram. Isotopic composition (in %; scaled on the right axis) is the blue line. Errors are less than the size of the symbol unless shown otherwise.

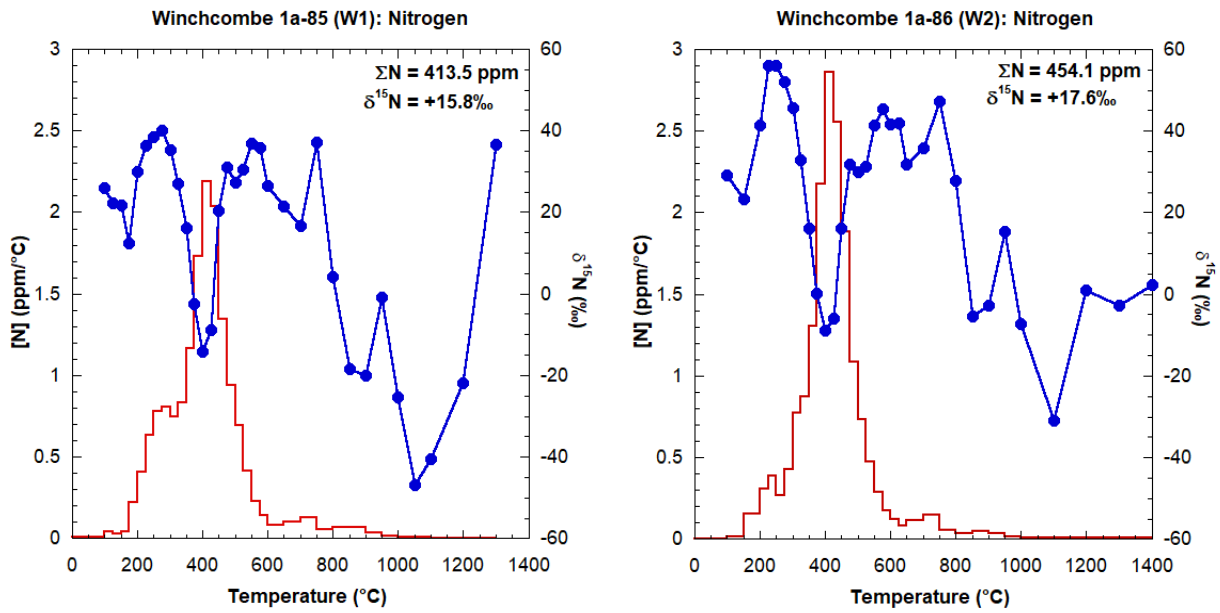

Figure S21. Nitrogen data from stepped combustion of Winchcombe chips BM.2022,M1-85 (5.0502 mg; 1a-85 (W1) on figure) and BM.2022,M1-86 (5.0981 mg; 1a-86 (W2) on figure). Abundance (in ppm $°C^{-1}$; scaled on the left axis) is the red histogram. Isotopic composition (in %; scaled on the right axis) is the blue line. Errors are less than the size of the symbol unless shown otherwise.

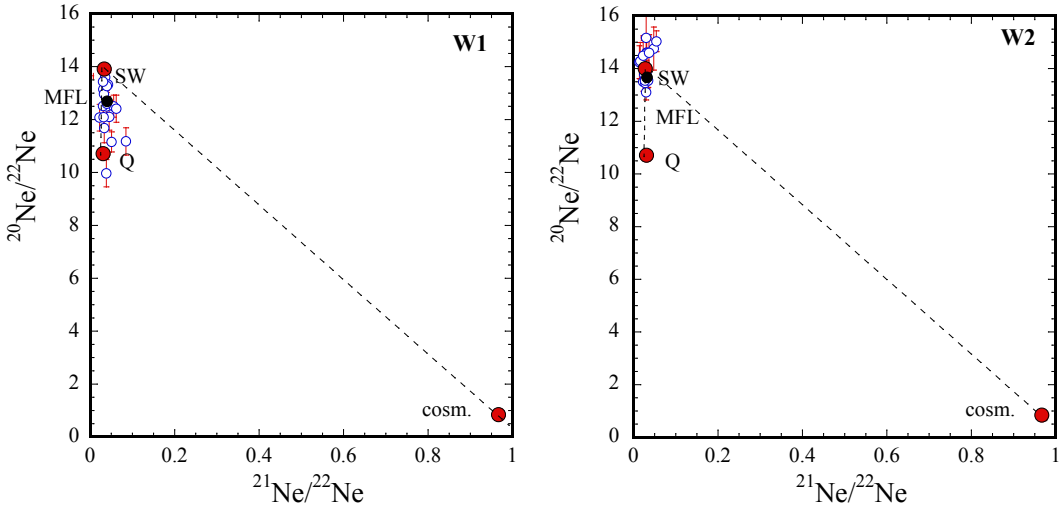

Figure S22. Isotopic composition of Ne in the temperature steps of Winchcombe meteorite samples BM.2022,M1-85 (W1) and BM.2022,M1-86 (W2). SW – solar wind composition (*121*); Q – planetary composition (*122*); MFL – mass fractionation line; cosm. – cosmogenic Ne. The total (summed) Ne isotopic composition is shown in black.

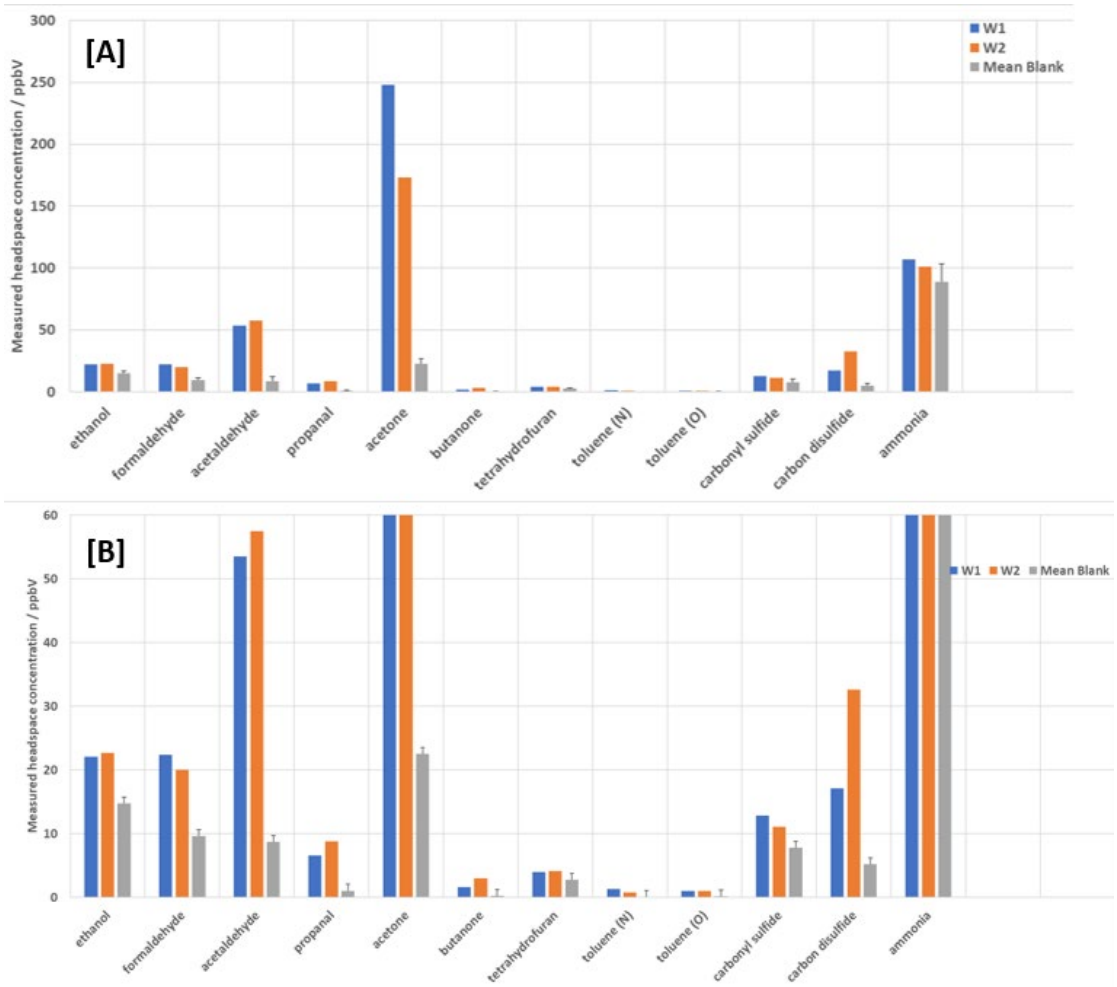

Figure S23. Species identified in a preliminary SIFT-MS analysis of headspace gases from Winchcombe meteorite samples BM.2022,M1-85 (W1, blue) and BM.2022,M1-86 (W2, orange). The blank from an empty vial is shown in grey. [A] Concentration in ppbV; [B] the same data at higher scale to show concentrations of minor species relative to the blank.

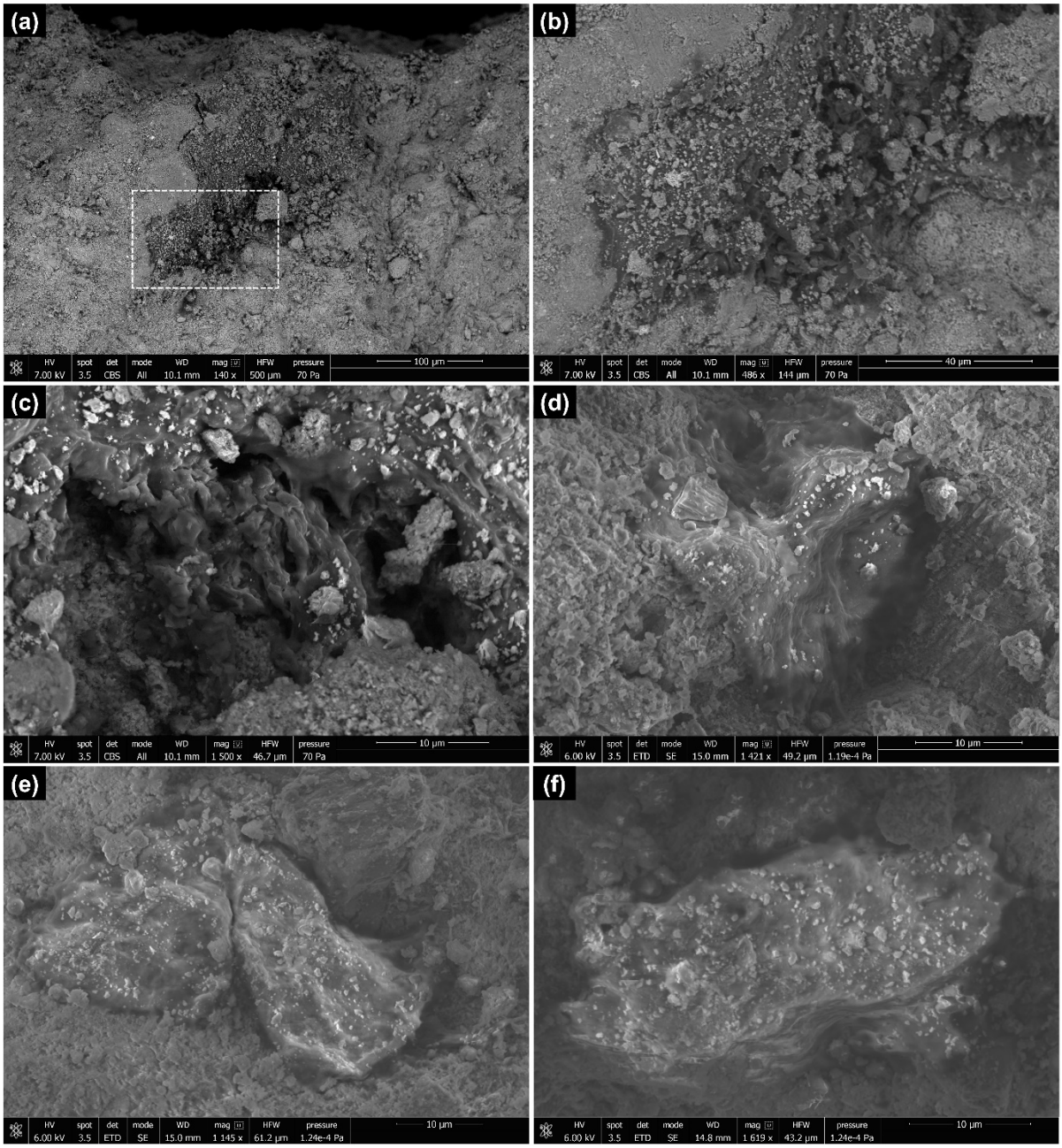

Figure S24. (a) BSE overview image of an ~100 × 300 µm carbon-rich area in a fragment of the Winchcombe meteorite. (b) BSE image of the area marked by a dashed white box in (a) showing that the carbon-rich area is intrinsic to the meteorite and not terrestrial contamination. (c) BSE image showing the texture of the carbon-rich material shown in (b). (d), (e), and (f) SE images of carbonaceous materials with "globule-like" morphologies found in uncoated and unprepared fragments of the Winchcombe meteorite.

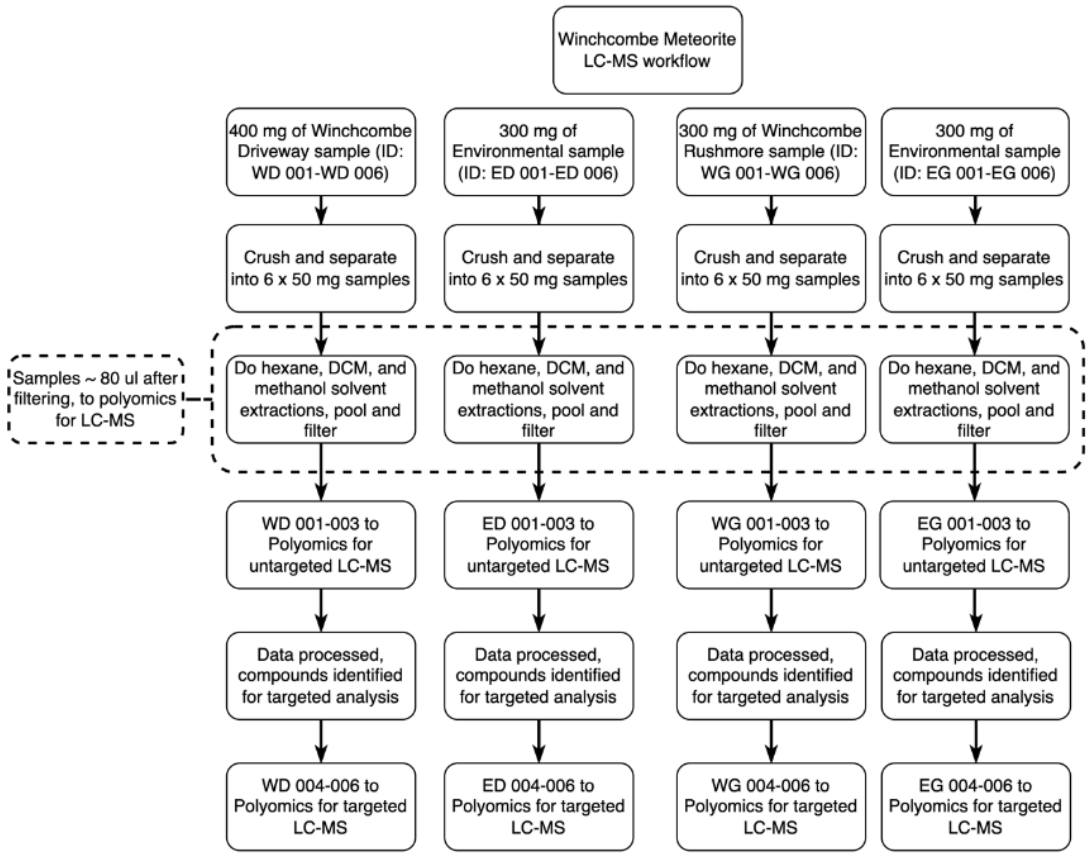

Figure S25. The analytical workflow for LC-MS characterization of the Winchcombe meteorite samples BM.2022,M2-23 and BM.2022,M9-4.

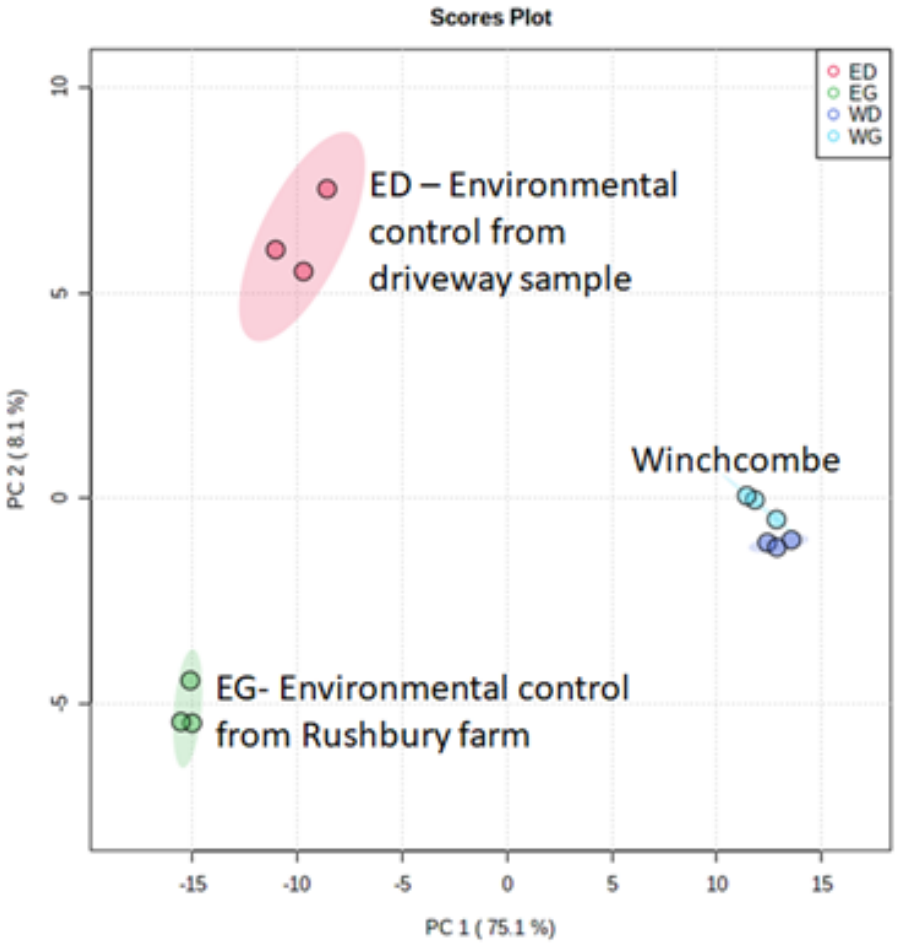

Figure S26. Two dimensional PCA of untargeted metabolomics data from the Winchcombe meteorite samples BM.2022,M2-23 and BM.2022,M9-4, and their corresponding environmental samples. The first principal component accounts for 75.1 % of the variance in the samples, indicating that the organic content in the solvent extracts of the Winchcombe meteorite was similar, but somewhat distinct from their environmental controls.

Table S1. Coordinates of UKFAll cameras that observed the Winchcombe fireball. Astrometry/Photometry indicates whether the data from the camera was used for astrometric picks (A) or for photometry (P).

Location	Network	Latitude (°)	Longitude (°)	Altitude (m, mean sea level)	Astrometry / Photometry
Cambridge	UKFN	52.164447	0.038883	8	-
Cardiff	SCAMP	51.486110	-3.177870	33	A + P
Chard	UKMON	50.877448	-2.949729	100	A
Chelmsford	NEMETODE	51.745000	0.493500	45	-
Clanfield	UKMON	50.938801	-1.019700	158	-
Honiton	SCAMP	50.801832	-3.184410	119	A + P
Hullavington	GMN	51.535053	-2.148658	103	A
Lincoln	UKFN	53.222048	-0.463622	16	A
Loughborough	NEMETODE	52.750500	-1.213000	73	-
Manchester	SCAMP	53.474365	-2.233606	69	P
Nuneaton	AllSky7	52.526389	-1.454722	80	-
Ringwood	GMN	50.857470	-1.778230	24	A
Tackley	GMN	51.883100	-1.306160	80	-
Welwyn	UKFN	51.268390	-0.394043	78	A
Wilcot	UKMON	51.351913	-1.801903	133	P
Antwerp (Bel)	AllSky7	51.213359	4.454574	16	-

Table S2. Radiant and pre-atmospheric orbit of the Winchcombe fireball.

Parameter		**Value**	1σ error	95% confidence interval	
Apparent radiant and entry velocity (relative to the ground)					
Azimuth (°)	A	263.342	± 0.046	263.235	263.399
Elevation (°)	a	41.919	± 0.029	41.852	41.961
Velocity (km/s)	v_0	13.547	± 0.008	13.531	13.560
Geocentric radiant (J2000.0) and velocity					
Right ascension (°)	α_G	56.638	± 0.017	56.604	56.671
Declination (°)	δ_G	+17.713	± 0.069	+17.555	+17.816
Velocity (km/s)	v_G	8.123	± 0.013	8.094	8.143
Heliocentric orbital elements (J2000.0)					
Semimajor axis (au)	a	2.5855	± 0.0077	2.5686	2.5980
Eccentricity	e	0.6183	± 0.0011	0.6158	0.6202
Perihelion distance (au)	q	0.986839	± 0.000012	0.986814	0.986861
Aphelion distance (au)	Q	4.184	± 0.015	4.150	4.209
Inclination (°)	i	0.460	± 0.014	0.440	0.491
Argument of perihelion (°)	ω	351.798	± 0.018	351.759	351.824
Ascending node (°)	Ω	160.1955	± 0.0014	160.1933	160.1985
Last perihelion		2021 Feb 22.446	± 0.015	2021 Feb 22.413	2021 Feb 22.469
Tisserand's parameter w.r.t. Jupiter	T_J	3.1207	± 0.0056	3.1117	3.1331

Table S3. Physical properties and atmospheric trajectory of the Winchcombe meteoroid.

	Initial	**Terminal**
Time (UTC)	21:54:15.88	21:54:24.12
Velocity (km/s)	13.54	~3
Latitude (°)	51.87106 ± 29 m	51.94011 ± 33 m
Longitude (°)	-3.10932 ± 17 m	-2.09634 ± 11 m
Height (km)	90.623 ± 38 m	27.554 ± 28 m
Mass (kg)	12.5 ± 3	~0.6
Observed length (km)	96.60	
Observed duration (s)	8.24	
Peak magnitude	-10.5^{M} at 53-55 km	
Peak dyn. pressure	0.6 MPa at 33.7 km	
Radiated energy	2.2×10^{7} J (0.005 T TNT)	

Table S4. Summary of recorded Winchcombe meteorite samples.

	Mass (g)	**Largest Fragment (g) / No. Fragments >1 g**	**Location**	**Finder**
Site 1: Winchcombe				
(M1) 01/03/21	206.5	8.8 / 44	Driveway / Lawn	Wilcock
(M2) 02/03/21	49.7	5.2 / 13	Driveway / Lawn	Wilcock
(M3) 04/03/21	39.5	7.3 / 1	Driveway / Lawn	Wilcock, King, Russell, Ensor
(M4) 05/03/21	23.0	6.2 / 2	Driveway / Lawn	Wilcock, Daly, Joy
(M5) 07/03/21	0.8	-	Driveway / Lawn	Wilcock, Suttle
Total Mass	*319.5*			
Site 2: Winchcombe				
(M6) 01/03/21	20.6	17.2 / 2	Driveway	Godfrey
Site 3: Woodmancote				
(M7) 02/03/21	11.2	11.2 / 1	Lawn	Carrick
Site 4: Woodmancote				
(M8) 05/03/21	20.1	13.7 / 2	Driveway	Mounsey
Site 5: Rushbury House				Ihasz, Daly, O'Brien, Hallis,
(M9) 06/03/21	160.1	152.0 / 1	Field	Bond
Site 6: Home Farm				Farrelly, Spencer, Naqvi,
(M10) 16/03/21	16.5	7.5 / 4	Field	Mayne, Skilton, Kirk
Total	**548.0**	152.0 / 70		

Table S5. Summary of fragments and powders of the Winchcombe meteorite analyzed in this study. Descriptions of the analytical techniques are given in the text.

Analysis	Sample ID	Parent Mass (g)	Institution
Fragments			
Major, minor & trace elements;	BM.2022,M1-91	0.3	NHM; Oxford
PSD-XRD; IR	BM.2022,M2-41	0.3	
Albedo	BM.2022,M1-22	2.0	Oxford
C, N & O isotopes	BM.2022,M1-85	8.8	OU
	BM.2022,M1-86	6.9	
Ti isotopes	BM.2022,M3-16	0.1	Bristol
Cr isotopes	BM.2022,M3-33	<0.1	St. Andrews
Ne isotopes; PSD-XRD	BM.2022,M2-36	0.3	SUERC; NHM
	BM.2022,M4-7	0.3	
Cosmogenic nuclides	BM.2022,M2-6	2.1	Gran Sasso
	OE-2021-23 (1)	3.2	Bratislava
	OE-2021-23 (7)	7.5	
	BM.2022,M2-40	0.1	Arizona
Magnetic properties	BM.2022,M1-95	0.1	Oxford/Cambridge
	BM.2022,M3-32		
H pyrolysis	BM.2022,M2-39	0.1	Glasgow/SUERC
GC-MS	BM.2022,M2-14	1.1	Imperial
LC-MS	BM.2022,M2-23	0.4	Glasgow
	BM.2022,M9-4	0.8	
Powders			
XRD; TGA	BM.2022,M1-88	0.2	NHM

Table S6. Neon isotope composition in Winchcombe meteorite samples BM.2022,M2-36 and BM.2022,M4-7.

Sample	$^{21}Ne/^{22}Ne$	$^{20}Ne/^{22}Ne$	$^{21}Ne_{cos}$ (cc/g)	CRE age	
1b-36				Ma	Ma
Step 1	0.0363 ± 0.0001	11.88 ± 0.02	1.76×10^{-10}		
			($\pm 2.22 \times 10^{-12}$)		
Step 2	0.0351 ± 0.0001	11.06 ± 0.02	6.17×10^{-11}		
			($\pm 1.17 \times 10^{-12}$)		
Step 3	0.0391 ± 0.0005	10.45 ± 0.02	1.95×10^{-11}		
			($\pm 1.04 \times 10^{-12}$)		
Step 4	0.0335 ± 0.0004	9.17 ± 0.01	5.90×10^{-12}		
			($\pm 9.04 \times 10^{-13}$)		
Total	0.0359 ± 0.0001	11.46 ± 0.02	2.63×10^{-10}	**0.212**	**0.085**
			($\pm 3.61 \times 10^{-12}$)	(± 0.0029)	(± 0.0012)
1d-8.2-6					
Step 1	0.1285 ± 0.0008	11.12 ± 0.02	1.60×10^{-10}		
			($\pm 1.19 \times 10^{-12}$)		
Step 2	0.0714 ± 0.0018	10.10 ± 0.04	4.04×10^{-11}		
			($\pm 1.77 \times 10^{-12}$)		
Step 3	0.0319 ± 0.0002	8.89 ± 0.01			
Step 4	0.0278 ± 0.0007	8.08 ± 0.02			
Total	0.0516 ± 0.0003	9.28 ± 0.01	1.89×10^{-10}	0.153	0.061
			($\pm 2.68 \times 10^{-12}$)	(± 0.0022)	(± 0.0009)

Table S7. Results of analysis of cosmogenic radionuclides in the Winchcombe meteorite.

Nuclide	Half-life	Activity (dpm kg^{-1})*			
		BM.2022,M2-6 INFN-LNGS Asergi	-23 (1) CU Bratislava	-23 (7) CU Bratislava	BM.2022,M2-40 AMS Tucson
^{7}Be	53.22 d	60 ± 20	< 190	110 ± 50	
^{58}Co	70.83 d	< 3	<14	< 6	
^{56}Co	77.236 d	5 ± 2	<9	8 ± 4	
^{46}Sc	83.788 d	8 ± 3	< 12	10 ± 5	
^{57}Co	271.8 d	< 11	<25	<17	
^{54}Mn	312.13 d	35 ± 4	39 ± 12	44 ± 6	
^{22}Na	2.6029 a	44 ± 5	36 ± 11	38 ± 7	
^{60}Co	5.2711 a	< 8	< 18	< 12	
^{44}Ti	60 y	< 13	<32	<19	
^{14}C	5730 a	-	-	-	13.3 ± 0.4
^{26}Al	7.17×10^{5} a	8 ± 2	14 ± 8	12 ± 5	

*) ^{14}C was analyzed by AMS, all other radionuclides by non-destructive gamma-ray spectrometry. Activities are corrected back to the date of the meteorite fall (28/2/2021). Uncertainties are given at 1σ. LNSG Asergi - Laboratori Nazionali del Gran Sasso; CU Bratislava - Department of Nuclear Physics and Biophysics of the Faculty of Mathematics, Physics and Informatics of the Comenius University; Tucson – National Science Foundation AMS Facility of the University of Arizona.

Table S8. Bulk major element composition (wt.%) of the Winchcombe meteorite measured by ICP-OES. Errors are the standard deviation of three replicate measurements.

	Winchcombe (BM.2022,M1-91)	**Winchcombe (BM.2022,M2-41)**
SiO_2	29.1 ± 0.4280	30.0 ± 0.1170
TiO_2	0.0972 ± 0.0004	0.0955 ± 0.0002
Al_2O_3	2.25 ± 0.0194	2.29 ± 0.0039
Fe_2O_3	31.7 ± 0.3700	32.1 ± 0.0529
MgO	18.1 ± 0.1470	17.8 ± 0.0372
CaO	1.79 ± 0.0067	1.57 ± 0.0072
Na_2O	0.565 ± 0.0035	0.616 ± 0.0015
P_2O_5	0.228 ± 0.0001	0.248 ± 0.0011
K_2O	0.0485 ± 0.0020	0.0604 ± 0.0004
MnO	0.21 ± 0.0009	0.207 ± 0.0005
NiO	1.55 ± 0.0085	1.56 ± 0.0036
Total	85.6	86.6

Table S9. Trace element abundances (ug g^{-1}) in the Winchcombe meteorite measured by ICP-MS. Errors are the standard deviation of three replicate measurements. < indicates that the abundance was below the limit of quantification.

	Winchcombe (BM.2022,M1-91)	**Winchcombe (BM.2022,M2-41)**
As	1.62 ± 0.0245	1.66 ± 0.0411
Ba	3.26 ± 0.0951	10.4 ± 0.2740
Be	<	<
Bi	<	<
Cd	0.396 ± 0.0078	0.39 ± 0.0089
Co	526 ± 4.28	521 ± 7.04
Cr	2572 ± 20.5	2561 ± 23.5
Cs	0.126 ± 0.0014	0.172 ± 0.0004
Cu	127 ± 0.5530	121 ± 1.6600
Ga	8.11 ± 0.0056	7.89 ± 0.0343
Ge	23.2 ± 0.0758	22.9 ± 0.2040
Hf	0.153 ± 0.0009	0.168 ± 0.0109
Li	1.39 ± 0.0200	1.65 ± 0.1080
Mo	1.16 ± 0.0048	1.04 ± 0.0061
Nb	0.345 ± 0.0005	0.343 ± 0.0038
Pb	1.46 ± 0.0215	1.44 ± 0.0346
Rb	1.68 ± 0.0469	2.0 ± 0.1020
Sb	0.106 ± 0.0009	0.106 ± 0.0030
Sc	7.65 ± 0.0271	9.7 ± 0.0377
Sn	<	<
Sr	10.2 ± 0.0543	9.97 ± 0.0320
Ta	<	<
Th	<	<
Tl	0.0883 ± 0.0025	0.0882 ± 0.0007
U	0.0108 ± 0.0002	0.0109 ± 0.0002
V	50.6 ± 1.2100	52.5 ± 0.4140
W	<	<
Y	1.85 ± 0.0081	2.05 ± 0.0111
Zn	168 ± 0.2410	173 ± 0.6480
Zr	4.7 ± 0.0328	5.27 ± 0.2680
La	0.398 ± 0.0326	0.37 ± 0.0076
Ce	0.996 ± 0.0175	1.51 ± 0.0106

Pr	0.13 ± 0.0008	0.132 ± 0.0015
Nd	0.66 ± 0.0038	0.662 ± 0.0141
Sm	0.209 ± 0.0082	0.201 ± 0.0071
Eu	0.0835 ± 0.0009	0.0821 ± 0.0008
Gd	0.276 ± 0.0015	0.283 ± 0.0040
Tb	0.0528 ± 0.0005	0.0577 ± 0.0004
Dy	0.358 ± 0.0058	0.419 ± 0.0133
Ho	0.078 ± 0.0008	0.0941 ± 0.0015
Er	0.235 ± 0.0064	0.258 ± 0.0008
Tm	0.0369 ± 0.0009	0.0364 ± 0.0011
Yb	0.237 ± 0.0028	0.23 ± 0.0037
Lu	0.00347 ± 0.0001	0.0354 ± 0.0002

Table S10. Oxygen isotopic composition of the Winchcombe meteorite samples BM.2022,M1-85 and BM.2022,M1-86.

	Weight (mg)	**$\delta^{17}O$(‰)**	1 σ	**$\delta^{18}O$ (‰)**	1 σ	**$\Delta^{17}O$ (‰)**	1 σ
M1-85-1	2.643	2.894	0.018	9.657	0.007	−2.128	0.020
M1-85-2	2.407	2.610	0.025	9.305	0.011	−2.229	0.027
average		*2.752*		*9.481*		*−2.178*	
M1-86-1	2.407	0.832	0.017	7.074	0.013	−2.846	0.020
M1-86-2	2.638	1.054	0.028	7.514	0.011	−2.853	0.034
average		*0.943*		*7.294*		*−2.850*	

Table S11. Titanium isotopic composition of the Winchcombe meteorite sample BM.2022,M3-16. Errors are 2σ.

Sample	n	$\Delta'^{46/47}Ti_{49/47}$ (ppm)	$\Delta'^{48/47}Ti_{49/47}$ (ppm)	$\Delta'^{50/47}Ti_{49/47}$ (ppm)
M3-16	10	46 ± 8	−4 ± 4	321 ± 9

Table S12. Chromium isotopic composition of the Winchcombe meteorite sample BM.2022,M3-33. Chromium isotope data are given in ε-units, which are the parts per ten thousand difference to the terrestrial standard NIST SRM 979.

Sample	n	$\varepsilon^{53}Cr_{50/52}$	2se	$\varepsilon^{54}Cr_{50/52}$	2se
M3-33	4	0.319	0.029	0.775	0.067
DTS2B	16	0.037	0.021	0.002	0.041

Table S13. Bulk modal mineralogy of the Winchcombe meteorite determined using PSD-XRD. PSF = total phyllosilicate abundance / [total anhydrous silicate + total phyllosilicate abundance].

	Winchcombe (M1-91)	**Winchcombe (M2-41)**	**Winchcombe (M2-36)**	**Average (1σ)**
Mg-serpentine	53.8	72.0	57.4	61.1 (9.6)
Fe-serpentine	33.7	21.1	30.0	28.3 (6.5)
Olivine	6.5	3.1	4.0	4.5 (1.8)
Pyroxene	1.6	-	2.6	2.1 (0.7)
Calcite	1.9	1.6	1.0	1.5 (0.5)
Magnetite	2.2	1.9	4.1	2.7 (1.2)
Sulphides	0.4	0.3	1.0	0.6 (0.4)
PSF	0.92	0.97	0.93	
Petrologic Type	1.2	1.1	1.2	

Table S14. Summary of polished sections of the Winchcombe meteorite characterized by SEM in this study. *Section P30554 mainly consisted of fusion crust.

Polished Section	Sample ID	Parent Mass (g)	Institution
P30423 (40.2 mm^2)	BM.2022,M1-87	0.3	
P30424 (7.5 mm^2)	BM.2022,M3-29	<0.1	
P30544 (2.5 mm^2)	BM.2022,M2-46	<0.1	NHM
P30548 (8.2 mm^2)	BM.2022,M1-105	<0.1	
P30553 (9.1 mm^2)	BM.2022,M9-15	<0.1	
P30540 (5.6 mm^2)	BM.2022,M2-42	<0.1	Glasgow
P30552 (9.8 mm^2)	BM.2022,M9-14	<0.1	
P30541 (12.2 mm^2)	BM.2022,M2-43	<0.1	Manchester
P30542 (7.8 mm^2)	BM.2022,M2-44	<0.1	Kent
P30543 (10.8 mm^2)	BM.2022,M2-45	<0.1	Leicester
P30545 (18.9 mm^2)	BM.2022,M2-47	<0.1	Plymouth
P30551 (7.4 mm^2)	BM.2022,M9-13	<0.1	Imperial
P30554 (5.1 mm^2)*	BM.2022,M9-16	<0.1	
P30555 (9.1 mm^2)	BM.2022,M9-17	<0.1	

Table S15. Representative composition (wt.%) of chondrule silicates, matrix and phyllosilicate clumps, pentlandite, tochilinite, and calcite measured by SEM-EDS in the main lithology of the Winchcombe meteorite. *n* is the number of analyses and values in parentheses are 1 standard deviation.

	Type I chondrule silicates	**Type II chondrule silicates**	**Matrix**	**Phyllosilicate clump (Fe-rich rim)**	**Phyllosilicate clump (Mg-rich core)**	**Pentlandite**	**Tochilinite**	**Calcite**
n	*42*	*8*	*61*	*106*	*78*	*46*	*3*	*49*
C								15.4 (3.1)
O	45.6 (1.7)	41.8 (1.8)	32.0 (2.2)	38.4 (4.4)	45.2 (7.0)	3.6 (3.4)	22.2 (0.7)	44.3 (2.5)
Na			0.8 (0.2)	0.5 (0.2)	0.5 (0.1)		0.1 (0.1)	
Mg	34.1 (1.8)	24.4 (3.7)	11.4 (1.8)	10.2 (1.5)	17.2 (0.7)	0.5 (1.0)	4.8 (2.6)	0.7 (0.9)
Al			0.9 (0.3)	1.3 (0.2)	1.0 (0.1)		0.4 (0.1)	0.1 (0.1)
Si	19.8 (0.8)	18.2 (0.8)	13.1 (1.4)	11.3 (1.1)	16.9 (0.8)	0.5 (0.9)	3.0 (3.4)	0.7 (0.9)
P			0.1 (0.1)				0.7 (0.6)	
S			2.6 (0.6)	5.3 (1.8)	1.5 (0.6)	30.7 (2.7)	19.1 (3.2)	0.2 (0.2)
Cl			0.2 (0.2)					
K							0.2 (0.1)	
Ca	0.3 (0.1)	0.1 (0.1)	0.2 (0.3)			0.1 (0.3)	0.1 (0.1)	37.6 (2.0)
Cr	0.3 (0.1)	0.3 (0.1)	0.3 (0.1)	0.2 (0.1)	0.1 (0.1)	0.3 (1.2)	0.9 (0.6)	
Mn	0.1 (0.1)	0.1 (0.1)	0.1 (0.1)	0.1 (0.1)	0.1 (0.1)		0.1 (0.1)	
Fe	1.4 (1.5)	16.5 (5.3)	13.5 (2.8)	26.0 (2.9)	10.9 (1.4)	32.8 (5.2)	35.7 (3.0)	1.0 (0.8)
Co						1.4 (1.0)	0.5 (0.3)	
Ni		0.1 (0.1)	1.6 (0.6)	0.9 (0.3)	0.5 (0.2)	29.0 (7.8)	9.1 (4.9)	
Total	101.5 (3.6)	101.6 (2.0)	76.7 (5.2)	94.3 (6.5)	94.0 (6.0)	99.1 (3.8)	96.7 (5.8)	100.0 (0.01)
Mg#	98.2 (2.0)	77.0 (8.1)	65.8 (7.3)	47.3 (6.0)	78.3 (2.5)		23.1 (10.5)	

Table S16. Summary of the bulk magnetic properties of the Winchcombe meteorite samples BM.2022,M1-95 and BM.2022,M3-32.

Sample	**M_S** ($Am^{-2}kg^{-1}$)	**M_{RS}** ($\times 10^{-3}$ $Am^{-2}kg^{-1}$)	**H_C** ($\times 10^{-3}$ T)	**H_{CR}** ($\times 10^{-3}$ T)	**log(χ)** ($\times 10^{-9}$ m^3 kg^{-1})	**S300 ratio**
M1-95	1.02	60.8	8.67	36.5	3.52	0.96
M3-32	0.10	6.98	9.74	38.3	3.03	0.95

Table S17. Mass loss (wt.%) as a function of temperature during TGA of the Winchcombe meteorite sample BM.2022,M1-88. The DTG curve is divided into temperature regions related to the dehydration of terrestrial adsorbed H_2O (15 - 200°C), the dehydration and dehydroxylation of Fe-(oxy)hydroxides (200 – 400°C) and phyllosilicates (400 – 770°C), and the breakdown of carbonates (770 – 900°C).

	15 - 200°C	**200 - 400°C**	**400 - 770°C**	**770 - 900°C**	**H_2O** (200 - 770°C)	**Fe-serpentine** (300 - 450°C)	**Mg-serpentine** (450 - 800°C)
Winchcombe (M1-88)	3.0	2.2	9.0	0.8	11.2	3.1	7.9

Table S18. Summary of the abundance and isotopic composition of hydrogen released during stepped pyrolysis of the Winchcombe meteorite samples BM.2022,M2-39-a, BM.2022,M2-39-b, and BM.2022,M2-39-c.

Winchcombe Sample No.	Step (°C)	H_2O (wt. %)	Fraction Released	H (wt. %)	δD (‰ vSMOW)
M2-39-a	100	0.29	0.03	0.03	−23
(45.1 mg)	200	1.20	0.11	0.13	−70
	300	1.32	0.12	0.15	−143
	400	2.79	0.26	0.31	−158
	500	2.91	0.27	0.33	−148
	700	1.91	0.18	0.21	−146
	1100	0.36	0.03	0.04	−43
	Total	**10.78**	**1.00**	**1.21**	
M2-39-b	100				
(32.7 mg)	200	0.92	0.08	0.10	−58
	300	1.17	0.10	0.13	−122
	400	3.11	0.27	0.35	−167
	500	2.74	0.23	0.31	−151
	700	2.95	0.25	0.33	−127
	1100	0.77	0.07	0.09	−55
	Total	**11.66**	**1.00**	**1.31**	
M2-39-c	100				
(30.9 mg)	200	0.86	0.07	0.10	−74
	300	1.13	0.09	0.13	−100
	400	2.97	0.24	0.33	−167
	500	3.17	0.26	0.36	−147
	700	3.14	0.26	0.35	−144
	1100	1.03	0.08	0.12	−74
	Total	**12.30**	**1.00**	**1.38**	

Table S19. Carbon data from stepped combustion of Winchcombe chips BM.2022,M1-85 and BM.2022,M1-86.

Temp (˚C)	[C] (ppm)	$\delta^{13}C$ (‰)	± σ (‰)	[C] (ppm)	$\delta^{13}C$ (‰)	±σ (‰)
	M1-85 (W1) 5.0502 mg			M1-86 (W2) 5.0981 mg		
100	56.6	3.1	0.2	19.7	-0.2	0.3
125	57.7	2.6	0.2			
150	60.8	0.5	0.1	135.1	2.0	0.2
175	100.2	5.6	0.4			
200	249.1	-8.0	0.3	288.1	-4.9	0.2
225	419.5	-6.0	0.7			
250	681.5	-2.7	0.1	891.8	13.1	5.0
275	963.0	2.4	0.7	670.4	8.7	0.9
300	1150.2	-3.6	0.3	825.0	-17.2	0.7
325	1324.3	-6.4	0.1	1505.8	-7.5	0.6
350	1456.4	-16.6	0.7	1543.2	-7.0	0.7
375	1593.3	-10.6	0.6	1658.1	-10.9	0.2
400	1874.9	-19.0	0.5	1728.8	-5.8	0.2
425	2043.1	-21.1	0.5	1836.1	-14.3	0.1
450	1862.3	-12.2	0.2	2123.1	-15.4	0.4
475	1268.3	-12.8	0.7	1670.8	-11.6	0.7
500	637.0	-9.6	0.7	1050.7	-9.0	0.3
525	260.6	-0.1	1.0	498.8	27.4	0.2
550	414.4	37.9	0.6	459.9	23.8	0.5
575	533.0	57.2	0.2	556.7	40.0	0.9
600	1099.4	61.5	0.2	1056.1	nm	
625				668.1	42.8	0.9
650	206.1	43.9	0.8	109.8	37.2	0.1
700	47.8	14.5	3.3	414.8	17.5	1.2
750	167.9	9.6	0.4	350.6	17.3	0.2
800	49.7	-8.9	1.1	122.7	nm	
850	42.3	17.4	0.1	60.8	nm	
900	21.5	5.7	1.8	54.7	48.9	5.0
950	19.0	26.5	1.5	64.2	55.8	0.9
1000	21.2	32.8	2.1	116.1	87.5	1.6
1050	31.4	65.0	2.5			
1100	18.7	60.4	0.4	98.6	142.5	1.2
1200	43.2	-19.9	0.1	54.2	12.6	0.2
1300	28.8	-16.3	0.2	34.7	-28.1	0.2
1400	20.4	-11.7	0.2	24.5	-19.3	0.2
Total:	18823.8	-2.8	0.1	20692.0	-0.6	0.1

Table S20. Nitrogen data from stepped combustion of Winchcombe chips BM.2022,M1-85 and BM.2022,M1-86.

Temp. (˚C)	[N] (ppm)	$\delta^{15}N$ (‰)	± σ (‰)	[N] (ppm)	$\delta^{15}N$ (‰)	± σ (‰)
	M1-85 (W1) 5.0502 mg			M1-86 (W2) 5.0981 mg		
100	0.9	25.9	0.2	0.5	29.3	0.4
125	1.0	22.3	0.2			
150	0.8	21.7	0.2	0.9	23.4	0.2
175	1.0	12.4	0.2			
200	5.5	30.1	0.2	7.8	41.4	0.2
225	10.2	36.3	0.2	7.7	56.0	0.2
250	15.8	38.4	0.2	9.7	56.1	0.2
275	19.4	40.1	0.2	6.7	51.9	0.2
300	20.1	35.3	0.2	10.6	45.5	0.2
325	18.6	27.1	0.2	19.3	32.9	0.2
350	20.7	16.2	0.2	21.8	16.2	0.2
375	29.0	-2.6	0.2	32.6	0.2	0.2
400	43.0	-14.1	0.2	54.4	-8.8	0.2
425	54.6	-8.8	0.2	71.5	-5.9	0.2
450	50.8	20.3	0.2	63.9	16.2	0.2
475	33.6	31.1	0.2	47.1	31.9	0.2
500	23.5	27.4	0.2	27.1	29.9	0.2
525	17.2	30.5	0.3	18.3	31.4	0.2
550	10.3	36.8	0.3	11.9	41.4	0.2
575	5.7	35.7	0.3	7.2	45.4	0.2
600	3.5	26.5	0.3	4.4	41.8	0.3
625				3.0	41.9	0.3
650	4.2	21.4	0.2	2.0	31.7	0.2
700	5.0	16.6	0.2	5.8	35.8	0.2
750	6.3	37.1	0.2	7.3	47.3	0.2
800	2.7	4.2	0.2	2.8	28.0	0.2
850	3.4	-18.4	0.2	1.9	-5.4	0.2
900	3.5	-19.9	0.2	2.3	-2.8	0.2
950	1.6	-1.0	0.2	1.7	15.4	0.3
1000	0.9	-25.3	0.2	0.9	-7.3	0.3
1050	0.5	-46.9	0.3			
1100	0.3	-40.4	0.3	0.9	-31.0	0.3
1200	0.2	-21.8	0.3	0.8	0.9	0.4
1300	0.0	36.7	0.4	0.7	-2.9	0.3
1400		nd		0.8	2.3	0.3
Total:	413.5	15.8	0.3	454.1	17.6	0.3

Table 21. He, Ne, Ar and Xe concentrations in the Winchcombe meteorite samples BM.2022,M1-85 and BM.2022,M1-86. nd – not determined.

Sample	^{4}He	^{20}Ne	^{36}Ar	^{132}Xe
		$\times 10^{-6}$ cm^3 STP g^{-1}		
M1-85 (W1)	145	3	2.87	nd
M1-86 (W2)	790	15	1.96	0.672

Table S22. The percentage of ammonium carbonate (A) and acetonitrile (B) flowing through the LC-MS column over time.

Time (mins)	% A	% B
0	20	80
15	80	20
15	95	5
17	95	5
17	20	80
26	20	80

Table S23. Summary of the amino acid content of the Winchcombe meteorite sample BM.2022,M2-14 and a soil sample collected near the fall site. n. f. indicates that the compound was not found in the sample above the detection limits.

	Winchcombe		**Fall Site Soil**	
	Free	Total	Free	Total
Glycine	131.7 ± 17.8	163.0 ± 17.2	13875 ± 181	54677 ± 402
D-Alanine	47.2 ± 2.2	57.0 ± 6.9	1595 ± 37	4957 ± 31
L-Alanine	46.4 ± 2.2	50.2 ± 5.1	34906 ± 607	54872 ± 458
β-Alanine	n. f.	28.3 ± 3.4	1389 ± 12	2869 ± 12
D-Serine	n. f.	n. f.	1695 ± 67	20629 ± 655
L-Serine	n. f.	n. f.	19627 ± 1266	68247 ± 5404
D-α-aminobutyric acid (ABA)	11.6 ± 1.4	12.6 ± 1.8	n. f.	n. f.
L-α-ABA	14.3 ± 1.2	16.7 ± 2.5	n. f.	n. f.
D-β-ABA	5.3 ± 3.4	8.0 ± 2.2	n. f.	n. f.
L-β-ABA	6.8 ± 3.2	12.8 ± 1.4	n. f.	n. f.
γ-ABA	n. f.	14.0 ± 2.3	1603 ± 25	2139 ± 21
α-aminoisobutyric acid (AIB)	467.1 ± 16.7	331.1 ± 33.6	n. f.	n. f.
D-β-AIB	n. f.	n. f.	n. f.	n. f.
L-β-AIB	n. f.	n. f.	n. f.	n. f.
D-Aspartic acid	6.7 ± 1.7	6.8 ± 0.7	1252 ± 15	10238 ± 33
L-Aspartic acid	12.7 ± 4.2	13.2 ± 1.6	18742 ± 206	82678 ± 472
D-Threonine	n. f.	n. f.	n. f.	n. f.
L-Threonine	n. f.	n. f.	20293 ± 273	40837 ± 284
D-Glutamic acid	<18.5	17.8 ± 3.0	1121 ± 21	5731 ± 34
L-Glutamic acid	<42.4	38.9 ± 4.1	26336 ± 229	84812 ± 705
D-Norvaline (2-apa)	3.0 ± 0.3	3.4 ± 0.6	n. f.	n. f.
L-Norvaline (2-apa)	2.7 ± 0.2	3.8 ± 0.8	n. f.	n. f.
D-Isovaline	196.7 ± 8.6	138.3 ± 14.7	n. f.	n. f.
L-Isovaline	194.4 ± 8.5	130.7 ± 13.9	n. f.	n. f.
D-Valine (2-a-3-mba)	9.2 ± 1.5	11.1 ± 1.5	n. f.	370 ± 0.2
L-Valine (2-a-3-mba)	16.6 ± 2.6	14.9 ± 1.5	28575 ± 477	30955 ± 153
R-3-Aminopentanoic acid (3-apa)	n. f.	n. f.	n. f.	n. f.
S-3-Aminopentanoic acid (3-apa)	n. f.	n. f.	n. f.	n. f.
D-4-amino-pentanoic acid (4-apa)	n. f.	n. f.	n. f.	n. f.
L-4-amino-pentanoic acid (4-apa)	n. f.	n. f.	n. f.	n. f.
5-Aminopentanoic acid (5-apa)	n. f.	20.3 ± 1.7	413 ± 11	847 ± 15
3-Amino-3-methyl butanoic acid	n. f.	n. f.	n. f.	n. f.

(3-a-3-mba)				
3-Amino-2,2-dimethylpropanoic acid (3-a-2,2-dmpa)	n. f.	n. f.	n. f.	n. f.
6-Amino-Hexanoic acid (eaca)	n. f.	28.6 ± 6.6	n. f.	n. f.
D-Norleucine	n. f.	n. f.	n. f.	n. f.
L-Norleucine	n. f.	n. f.	n. f.	n. f.
D-isoleucine	n. f.	n. f.	n. f.	n. f.
L-isoleucine	n. f.	n. f.	16639 ± 256	15752 ± 43
D-Leucine	5.0 ± 0.8	4.1 ± 0.1	n. f.	n. f.
L-Leucine	9.7 ± 1.5	6.5 ± 1.0	38345 ± 537	26979 ± 71
L-Alloisoleucine	n. f.	n. f.	n. f.	n. f.
D-2-Methylleucine	n. f.	n. f.	n. f.	n. f.
D-2-Aminoheptanoic acid (2-aha)	n. f.	n. f.	n. f.	n. f.
L-2-Aminoheptanoic acid (2-aha)	n. f.	n. f.	n. f.	n. f.
Total	**1247.9 ± 30.9**	**1132.3 ± 49.3**	**226406 ± 1662**	**507587 ± 5553**

REFERENCES AND NOTES

1. T. S. Kruijer, C. Burkhardt, G. Budde, T. Kleine, Age of Jupiter inferred from the distinct genetics and formation times of meteorites. *Proc. Natl. Acad. Sci. U.S.A.* **114**, 6712–6716 (2017).

2. T. Lichtenberg, J. Drążkowska, M. Schöbächler, G. J. Golabek, T. O. Hands, Bifurcation of planetary building blocks during solar system formation. *Science* **371**, 365–370 (2021).

3. K. J. Walsh, A. Morbidelli, S. N. Raymond, D. P. O'Brien, A. M. Mandell, Populating the asteroid belt from two parent source regions due to the migration of giant planets—"The Grand Tack". *Meteorit. Planet. Sci.* **47**, 1941–1947 (2012).

4. F. E. DeMeo, B. Carry, Solar system evolution from compositional mapping of the asteroid belt. *Nature* **505**, 629–634 (2014).

5. C. M. O'D. Alexander, R. Bowden, M. L. Fogel, K. T. Howard, C. D. K. Herd, L. R. Nittler, The provenances of asteroids, and their contributions to the volatile inventories of the terrestrial planets. *Science* **337**, 721–723 (2012).

6. P. G. Brown, A. R. Hildebrand, M. E. Zolensky, M. Grady, R. N. Clayton, T. K. Mayeda, E. Tagliaferri, R. Spalding, N. D. MacRae, E. L. Hoffman, D. W. Mittlefehldt, J. F. Wacker, J. A. Bird, M. D. Campbell, R. Carpenter, H. Gingerich, M. Glatiotis, E. Greiner, M. J. Mazur, P. J. A. McCausland, H. Plotkin, T. R. Mazur, The fall, recovery, orbit, and composition of the Tagish Lake meteorite: A new type of carbonaceous chondrite. *Science* **290**, 320–325 (2000).

7. P. Jenniskens, M. D. Fries, Q.-Z. Yin, M. Zolensky, A. N. Krot, S. A. Sandford, D. Sears, R. Beauford, D. S. Ebel, J. M. Friedrich, K. Nagashima, J. Wimpenny, A. Yamakawa, K. Nishiizumi, Y. Hamajima, M. W. Caffee, K. C. Welten, M. Laubenstein, A. M. Davis, S. B. Simon, P. R. Heck, E. D. Young, I. E. Kohl, M. H. Thiemens, M. H. Nunn, T. Mikouchi, K. Hagiya, K. Ohsumi, T. A. Cahill, J. A. Lawton, D. Barnes, A. Steele, P. Rochette, K. L. Verosub, J. Gattacceca, G. Cooper, D. P. Glavin, A. S. Burton, J. P. Dworkin, J. E. Elsila, S. Pizzarello, R. Ogliore, P. Schmitt-Kopplin, M. Harir, N. Hertkorn, A. Verchovsky, M. Grady, K. Nagao, R. Okazaki, H. Takechi, T. Hiroi, K. Smith, E. A. Silber, P. G. Brown, J. Albers, D. Klotz, M. Hankey, R. Matson, J. A. Fries, R. J. Walker, I. Puchtel, C-T. A. Lee, M. E. Erdman, G. R. Eppich, S. Roeske, Z. Gabelica, M. Lerche, M.

Nuevo, B. Girten, S. P. Worden, Radar-enabled recovery of the Sutter's Mill meteorite, a carbonaceous chondrite regolith breccia. *Science* **338**, 1583–1587 (2012).

8. J. Borovička, O. Popova, P. Spurný, The Maribo CM2 meteorite fall—Survival of weak material at high entry speed. *Meteorit. Planet. Sci.* **54**, 1024–1041 (2019).

9. J. Borovička, F. Bettonvil, G. Baumgarten, J. Strunk, M. Hankey, P. Spurný, D. Heinlein, Trajectory and orbit of the unique carbonaceous meteorite Flensburg. *Meteorit. Planet. Sci.* **56**, 425–439 (2021).

10. W. F. Bottke, D. Vokrouhlický, K. J. Walsh, M. Delbo, P. Michel, D. S. Lauretta, H. Campins, H. C. Connolly Jr., D. J. Scheeres, S. R. Chelsey, In search of the source of asteroid (101955) Bennu: Applications of the stochastic YORP model. *Icarus* **247**, 191–217 (2015).

11. T. Morota, S. Sugita, Y. Cho, M. Kanamaru, E. Tatsumi, N. Sakatani, R. Honda, N. Hirata, H. Kikuchi, M. Yamada, Y. Yokota, S. Kameda, M. Matsuoka, H. Sawada, C. Honda, T. Kouyama, K. Ogawa, H. Suzuki, K. Yoshioka, M. Hayakawa, N. Hirata, M. Hirabayashi, H. Miyamoto, T. Michikami, T. Hiroi, R. Hemmi, O.S. Barnouin, C.M. Ernst, K. Kitazato, T. Nakamura, L. Riu, H. Senshu, H. Kobayashi, S. Sasaki, G. Komatsu, N. Tanabe, Y. Fujii, T. Irie, M. Suemitsu, N. Takaki, C. Sugimoto, K. Yumoto, M. Ishida, H. Kato, K. Moroi, D. Domingue, P. Michel, C. Pilorget, T. Iwata, M. Abe, M. Ohtake, Y. Nakauchi, K. Tsumura, H. Yabuta, Y. Ishihara, R. Noguchi, K. Matsumoto, A. Miura, N. Namiki, S. Tachibana, M. Arakawa, H. Ikeda, K. Wada, T. Mizuno, C. Hirose, S. Hosoda, O. Mori, T. Shimada, S. Soldini, R. Tsukizaki, H. Yano, M. Ozaki, H. Takeuchi, Y. Yamamoto, T. Okada, Y. Shimaki, K. Shirai, Y. Iijima, H. Noda, S. Kikuchi, T. Yamaguchi, N. Ogawa, G. Ono, Y. Mimasu, K. Yoshikawa, T. Takahashi, Y. Takei, A. Fujii, S. Nakazawa, F. Terui, S. Tanaka, M. Yoshikawa, T. Saiki, S. Watanabe, Y. Tsuda, Sample collection from asteroid (162173) Ryugu by Hayabusa2: Implications for surface evolution. *Science* **368**, 654–659 (2020).

12. M. Granvik, P. Brown, Identification of meteorite source regions in the solar system. *Icarus* **311**, 271–287 (2018).

13. P. M. Schober, E. K. Sansom, P. A. Bland, H. A. R. Devillepoix, M. C. Towner, M. Cupák, R. M. Howie, B. A. D. Hartig, S. L. Anderson, The main asteroid belt: The primary source of debris on

comet-like orbits. *Planet. Sci.* **2**, 98 (2021).

14. P. Farinella, D. Vokrouhlický, W. K. Hartmann, Meteorite delivery via Yarkovsky orbital drift, *Icarus* **132**, 378–387 (1998).

15. D. Krietsch, H. Busemann, M. E. I. Riebe, A. J. King, C. M. O'D. Alexander, C. Maden, Noble gases in CM carbonaceous chondrites: Effect of parent body aqueous and thermal alteration and cosmic ray exposure ages. *Geochim. Cosmochim. Acta* **310**, 240–280 (2021).

16. J. Borovička, P. Spurný, L. Shrbený, Two strengths of ordinary chondritic meteoroids as derived from their atmospheric fragmentation modeling. *Astronom. J.* **160**, 42 (2020).

17. R. N. Clayton, T. K. Mayeda, Oxygen isotope studies of carbonaceous chondrites. *Geochim. Cosmochim. Acta* **63**, 2089–2104 (1999).

18. D. L. Schrader, I. A. Franchi, H. C. Connolly Jr., R. C. Greenwood, D. S. Lauretta, J. M. Gibson, The formation and alteration of the Renazzo-like carbonaceous chondrites I: Implications of bulk-oxygen isotopic composition. *Geochim. Cosmochim. Acta* **75**, 308–325 (2011).

19. E. Tonui, M. Zolensky, T. Hiroi, T. Nakamura, M. E. Lipschutz, M.-S. Wang, K. Okudaira, Petrographic, chemical and spectroscopic evidence for thermal metamorphism in carbonaceous chondrites I: CI and CM chondrites. *Geochim. Cosmochim. Acta* **126**, 284–306 (2014).

20. K. Tomeoka, P. R. Buseck, Indicators of aqueous alteration in CM carbonaceous chondrites: Microtextures of a layered mineral containing Fe, S, O and Ni. *Geochim. Cosmochim. Acta* **49**, 2149–2163 (1985).

21. A. E. Rubin, J. M. Trigo-Rodríguez, H. Huber, J. T. Wasson, Progressive aqueous alteration of CM carbonaceous chondrites. *Geochim. Cosmochim. Acta* **71**, 2361–2382 (2007).

22. P. Michel, R.-L. Ballouz, O. S. Barnouin, M. Jutzi, K. J. Walsh, B. H. May, C. Manzoni, D. C. Richardson, S. R. Schwartz, S. Sugita, S. Watanabe, H. Miyamoto, M. Hirabayashi, W. F. Bottke, H. C. Connolly, M. Yoshikawa, D. S. Lauretta, Collisional formation of top-shaped asteroids and implications for the origins of Ryugu and Bennu. *Nat. Commun.* **11**, 2655 (2020).

23. C. M. O'D. Alexander, K. T. Howard, R. Bowden, M. L. Fogel, The classification of CM and CR chondrites using bulk H, C and N abundances and isotopic compositions. *Geochim. Cosmochim. Acta* **123**, 244–260 (2013).

24. L. G. Vacher, L. Piani, T. Rigaudier, D. Thomassin, G. Florin, M. Piralla, Y. Marrocchi, Hydrogen in chondrites: Influence of parent body alteration and atmospheric contamination on primordial components. *Geochim. Cosmochim. Acta* **281**, 53–66 (2020).

25. M. R. Lee, B. E. Cohen, A. J. Boyce, L. J. Hallis, L. Daly, The pre-atmospheric hydrogen inventory of CM carbonaceous chondrites. *Geochim. Cosmochim. Acta* **309**, 31–44 (2021).

26. M. R. Lee, L. Daly, C. Floyd, P.-E. Martin, CM carbonaceous chondrite falls and their terrestrial alteration. *Meteorit. Planet. Sci.* **56**, 34–48 (2021).

27. E. T. Peltzer, J. L. Bada, G. Schlesinger, S. L. Miller, The chemical conditions on the parent body of the Murchison meteorite: Some conclusions based on amino, hydroxy and dicarboxylic acids. *Adv. Space Res.* **4**, 69–74 (1984).

28. O. Botta, Z. Martins, P. Ehrenfreund, Amino acids in Antarctic CM1 meteorites and their relationship to other carbonaceous chondrites. *Meteorit. Planet. Sci.* **42**, 81–92 (2007).

29. D. P. Glavin, M. P. Callahan, J. P. Dworkin, J. E. Elsila, The effects of parent body processes on amino acids in carbonaceous chondrites. *Meteorit. Planet. Sci.* **45**, 1948–1972 (2011).

30. J. R. Cronin, S. Pizzarello, Enantiomeric excesses in meteoritic amino acids. *Science* **275**, 951–955 (1997).

31. D. P. Glavin, J. E. Elsila, H. L. Mclain, J. C. Aponte, E. T. Parker, J. P. Dworkin, D. H. Hill, H. C. Connolly Jr., D. S. Lauretta, Extraterrestrial amino acids and L-enantiomeric excesses in the CM2 carbonaceous chondrites Aguas Zarcas and Murchison. *Meteorit. Planet. Sci.* **56**, 148–173 (2021).

32. H. A. R. Devillepoix, M. Cupák, P. A. Bland, E. K. Sansom, M. C. Towner, R. M. Howie, B. A. D. Hartig, T. Jansen-Sturgeon, P. M. Shober, S. L. Anderson, G. K. Benedix, A global fireball observatory. *Planet. Space Sci.* **191**, 105036 (2020).

33. F. Colas, B. Zanda, S. Bouley, S. Jeanne, A. Malgoyre, M. Birlan, C. Blanpain, J. Gattacceca, L. Jorda, J. Lecubin, C. Marmo, J. L. Rault, J. Vaubaillon, P. Vernazza, C. Yohia, D. Gardiol, A. Nedelcu, B. Poppe, J. Rowe, M. Forcier, D. Koschny, J. M. Trigo-Rodriguez, H. Lamy, R. Behrend, L. Ferrière, D. Barghini, A. Buzzoni, A. Carbognani, M. di Carlo, M. di Martino, C. Knapic, E. Londero, G. Pratesi, S. Rasetti, W. Riva, G.M. Stirpe, G.B. Valsecchi, C.A. Volpicelli, S. Zorba, D. Coward, E. Drolshagen, G. Drolshagen, O. Hernandez, E. Jehin, M. Jobin, A. King, C. Nitschelm, T. Ott, A. Sanchez-Lavega, A. Toni, P. Abraham, F. Affaticati, M. Albani, A. Andreis, T. Andrieu, S. Anghel, E. Antaluca, K. Antier, T. Appéré, A. Armand, G. Ascione, Y. Audureau, G. Auxepaules, T. Avoscan, D. B. Aissa, P. Bacci, O. Bădescu, R. Baldini, R. Baldo, A. Balestrero, D. Baratoux, E. Barbotin, M. Bardy, S. Basso, O. Bautista, L. D. Bayle, P. Beck, R. Bellitto, R. Belluso, C. Benna, M. Benammi, E. Beneteau, Z. Benkhaldoun, P. Bergamini, F. Bernardi, M.E. Bertaina, P. Bessin, L. Betti, F. Bettonvil, D. Bihel, C. Birnbaum, O. Blagoi, E. Blouri, I. Boacă, R. Boată, B. Bobiet, R. Bonino, K. Boros, E. Bouchet, V. Borgeot, E. Bouchez, D. Boust, V. Boudon, T. Bouman, P. Bourget, S. Brandenburg, P. Bramond, E. Braun, A. Bussi, P. Cacault, B. Caillier, A. Calegaro, J. Camargo, S. Caminade, A. P. C. Campana, P. Campbell-Burns, R. Canal-Domingo, O. Carell, S. Carreau, E. Cascone, C. Cattaneo, P. Cauhape, P. Cavier, S. Celestin, A. Cellino, M. Champenois, H. C. Aoudjehane, S. Chevrier, P. Cholvy, L. Chomier, A. Christou, D. Cricchio, P. Coadou, J. Y. Cocaign, F. Cochard, S. Cointin, E. Colombi, J. P. Colque Saavedra, L. Corp, M. Costa, F. Costard, M. Cottier, P. Cournoyer, E. Coustal, G. Cremonese, O. Cristea, J. C. Cuzon, G. D'Agostino, K. Daiffallah, C. Dănescu, A. Dardon, T. Dasse, C. Davadan, V. Debs, J. P. Defaix, F. Deleflie, M. D'Elia, P. de Luca, P. de Maria, P. Deverchère, H. Devillepoix, A. Dias, A. di Dato, R. di Luca, F. M. Dominici, A. Drouard, J. L. Dumont, P. Dupouy, L. Duvignac, A. Egal, N. Erasmus, N. Esseiva, A. Ebel, B. Eisengarten, F. Federici, S. Feral, G. Ferrant, E. Ferreol, P. Finitzer, A. Foucault, P. Francois, M. Frîncu, J.L. Froger, F. Gaborit, V. Gagliarducci, J. Galard, A. Gardavot, M. Garmier, M. Garnung, B. Gautier, B. Gendre, D. Gerard, A. Gerardi, J.P. Godet, A. Grandchamps, B. Grouiez, S. Groult, D. Guidetti, G. Giuli, Y. Hello, X. Henry, G. Herbreteau, M. Herpin, P. Hewins, J. J. Hillairet, J. Horak, R. Hueso, E. Huet, S. Huet, F. Hyaumé, G. Interrante, Y. Isselin, Y. Jeangeorges, P. Janeux, P. Jeanneret, K. Jobse, S. Jouin, J. M. Jouvard, K. Joy, J. F. Julien, R. Kacerek, M. Kaire, M. Kempf, D. Koschny, C. Krier, M. K. Kwon, L. Lacassagne, D. Lachat, A. Lagain, E. Laisné, V. Lanchares, J. Laskar, M. Lazzarin, M. Leblanc, J. P. Lebreton, J. Lecomte, P. le Dû, F. Lelong, S. Lera, J. F. Leoni, A. le-Pichon, P. le-Poupon, A. Leroy, G. Leto, A. Levansuu, E. Lewin, A. Lienard, D. Licchelli, H. Locatelli, S. Loehle, D. Loizeau, L. Luciani, M. Maignan, F. Manca, S. Mancuso, E. Mandon, N. Mangold, F. Mannucci, L. Maquet, D. Marant, Y. Marchal, J. L. Marin, J. C. Martin-Brisset, D. Martin, D. Mathieu, A. Maury, N. Mespoulet, F. Meyer, J. Y. Meyer, E. Meza, V. Moggi Cecchi, J. J. Moiroud, M. Millan, M. Montesarchio, A. Misiano, E. Molinari, S. Molau, J. Monari, B. Monflier, A. Monkos, M. Montemaggi, G. Monti, R. Moreau, J. Morin, R. Mourgues, O. Mousis, C. Nablanc, A. Nastasi, L. Niacşu, P. Notez, M. Ory, E. Pace, M. A. Paganelli, A. Pagola, M. Pajuelo, J.F. Palacián, G. Pallier, P. Paraschiv, R. Pardini, M. Pavone, G. Pavy, G. Payen, A. Pegoraro, E. Peña-Asensio, L. Perez, S. Pérez-Hoyos, V. Perlerin, A. Peyrot, F. Peth, V. Pic, S. Pietronave, C. Pilger, M. Piquel, T. Pisanu, M. Poppe, L. Portois, J. F. Prezeau, N. Pugno, C. Quantin, G. Quitté, N. Rambaux, E. Ravier, U. Repetti, S. Ribas, C. Richard, D. Richard, M. Rigoni, J. P. Rivet, N. Rizzi, S. Rochain, J. F. Rojas, M. Romeo, M. Rotaru, M. Rotger, P. Rougier, P. Rousselot, J. Rousset, D. Rousseu, O. Rubiera, R. Rudawska, J. Rudelle, J. P. Ruguet, P. Russo, S. Sales, O. Sauzereau, F. Salvati, M. Schieffer, D. Schreiner, Y. Scribano, D. Selvestrel, R. Serra, L. Shengold, A. Shuttleworth, R. Smareglia, S. Sohy, M. Soldi, R. Stanga, A. Steinhausser, F. Strafella, S. S. Mbaye, A. R. D. Smedley, M. Tagger, P. Tanga, C. Taricco, J. P. Teng, J. O. Tercu, O. Thizy,

J. P. Thomas, M. Tombelli, R. Trangosi, B. Tregon, P. Trivero, A. Tukkers, V. Turcu, G. Umbriaco, E. Unda-Sanzana, R. Vairetti, M. Valenzuela, G. Valente, G. Varennes, S. Vauclair, J. Vergne, M. Verlinden, M. Vidal-Alaiz, R. Vieira-Martins, A. Viel, D. C. Vîntdevară, V. Vinogradoff, P. Volpini, M. Wendling, P. Wilhelm, K. Wohlgemuth, P. Yanguas, R. Zagarella, A. Zollo, FRIPON: A worldwide network to track incoming meteoroids. *Astron. Astrophys.* **644**, A53 (2020).

34. D. Vida, D. Šegon, P. S. Gural, P. G. Brown, M. J. McIntyre, T. J. Dijkema, L. Pavletić, P. Kukić, M. J. Mazur, P. Eschman, P. Roggemans, A. Merlak, D. Zubović, The Global Meteor Network—Methodology and first results. *Mon. Notices Royal Astron. Soc.* **506**, 5046–5074 (2021).

35. M. Hankey, V. Perlerin, D. Meisel, The all-sky-6 and the Video Meteor Archive system of the AMS Ltd. *Planet. Space Sci.* **190**, 105005 (2020).

36. T. J. Warren, N. E. Bowles, K. Donaldson Hanna, I. R. Thomas, The Oxford Space Environment Goniometer: A new experimental setup for making directional emissivity measurements under a simulated space environment. *Rev. Sci. Instr.* **88**, 124502 (2017).

37. B. Hapke, Bidirectional reflectance spectroscopy 7: The single particle phase function hockey stick relation. *Icarus* **221**, 1079–1083 (2012).

38. D. Györe, L. Di Nicola, D. Currie, F. M. Stuart, New system for measuring cosmogenic Ne in terrestrial and extra-terrestrial rocks. *Geosci.* **11**, 353 (2021).

39. P. P. Povinec, I. Sýkora, V. Porubčan, M. Ješkovský, Analysis of ^{26}Al in meteorite samples by coincidence gamma-ray spectrometry. *J. Radioanal. Nucl. Chem.* **282**, 805–808 (2009).

40. P. P. Povinec, I. Sýkora, A. Kováčik, C. Koeberl, High-sensitivity HPGe gamma-spectrometry analysis of radionuclides in Martian meteorites. *J. Radioanal. Nucl. Chem.* **307**, 2403–2407 (2016).

41. M. Laubenstein, Screening of materials with high purity germanium detectors at the Laboratori Nazionali del Gran Sasso. *Intern. J. Modern Phys. A* **32**, 1743002 (2017).

42. S. Agostinelli, J. Allison, K. Amako, J. Apostolakis, H. Araujo, P. Arce, M. Asai, D. Axen, S. Banerjee, G. Barrand, F. Behner, L. Bellagamba, J. Boudreau, L. Broglia, A. Brunengo, H. Burkhardt, S. Chauvie, J. Chuma, R. Chytracek, G. Cooperman, G. Cosmo, P. Degtyarenko, A. Dell'Acqua, G. Depaola, D. Dietrich, R. Enami, A. Feliciello, C. Ferguson, H. Fesefeldt, G. Folger,

F. Foppiano, A. Forti, S. Garelli, S. Giani, R. Giannitrapani, D. Gibin, J.J. Gómez Cadenas, I. González, G. Gracia Abril, G. Greeniaus, W. Greiner, V. Grichine, A. Grossheim, S. Guatelli, P. Gumplinger, R. Hamatsu, K. Hashimoto, H. Hasui, A. Heikkinen, A. Howard, V. Ivanchenko, A. Johnson, F. W. Jones, J. Kallenbach, N. Kanaya, M. Kawabata, Y. Kawabata, M. Kawaguti, S. Kelner, P. Kent, A. Kimura, T. Kodama, R. Kokoulin, M. Kossov, H. Kurashige, E. Lamanna, T. Lampén, V. Lara, V. Lefebure, F. Lei, M. Liendl, W. Lockman, F. Longo, S. Magni, M. Maire, E. Medernach, K. Minamimoto, P. Mora de Freitas, Y. Morita, K. Murakami, M. Nagamatu, R. Nartallo, P. Nieminen, T. Nishimura, K. Ohtsubo, M. Okamura, S. O'Neale, Y. Oohata, K. Paech, J. Perl, A. Pfeiffer, M. G. Pia, F. Ranjard, A. Rybin, S. Sadilov, E. di Salvo, G. Santin, T. Sasaki, N. Savvas, Y. Sawada, S. Scherer, S. Sei, V. Sirotenko, D. Smith, N. Starkov, H. Stoecker, J. Sulkimo, M. Takahata, S. Tanaka, E. Tcherniaev, E. Safai Tehrani, M. Tropeano, P. Truscott, H. Uno, L. Urban, P. Urban, M. Verderi, A. Walkden, W. Wander, H. Weber, J. P. Wellisch, T. Wenaus, D.C. Williams, D. Wright, T. Yamada, H. Yoshida, D. Zschiesche, GEANT 4—A simulation toolkit. *Nucl. Instrum. Meth. Phys. A* **506**, 250–303 (2003).

43. A. J. T. Jull, L. R. McHargue, P. A. Bland, R. C. Greenwood, W. R. Bevan, K. J. Kim, M. D. Giscard, S. E. LaMotta, J. A. Johnson, Terrestrial ages of meteorites from the Nullarbor region, Australia, based on ^{14}C and ^{14}C-^{10}Be measurements. *Meteorit. Planet. Sci.* **45**, 1271–1283 (2010).

44. LNHB, Laboratoire National Henry Becquerel. 2013. Nucleide; www.nucleide.org.

45. M. F. Miller, I. A. Franchi, A. S. Sexton, C. T. Pillinger, High precision Δ^{17}O isotope measurements of oxygen from silicates and other oxides: Method and applications. *Rapid. Commun. Mass Spec.* **13**, 1211–1217 (1999).

46. D. L. Schrader, J. Davidson, R. C. Greenwood, I. A Franchi, J. M. A. Gibson, A water-ice rich minor body from the early solar system: The CR chondrite parent asteroid. *Earth Planet. Sci. Lett.* **407**, 48–60 (2014).

47. N. A. Starkey, C. R. M. Jackson, R. C. Greenwood, S. Parman, I. A. Franchi, M. Jackson, J. G. Fitton, F. M. Stuart, M. Kurz, L. M. Larsen, Triple oxygen isotopic composition of the high ^{3}He/^{4}He mantle. *Geochim. Cosmochim. Acta* **176**, 227–238 (2016).

48. F. R. Niederer, D. A. Papanastassiou, G. J. Wasserburg, The isotopic composition of titanium in the Allende and Leoville meteorites. *Geochim. Cosmochim. Acta* **45**, 1017–1031 (1981).

49. W. A. Russell, D. A. Papanastassiou, T. A. Tombrello, Ca isotope fractionation on the Earth and other solar system materials. *Geochim. Cosmochim. Acta* **42**, 1075–1090 (1978).

50. G. D. Flesch, J. Capellen, H. J. Svec, *Advanced Mass Spectrometry III* (1966), pp. 571–581.

51. W. R. Shields, T. J. Murphy, E. J. Catanzaro, E. L. Garner, Absolute isotopic abundance ratios and the atomic weight of a reference sample of chromium. *J. Res. Natl. Bur. Stand. A* **70**, 193–197 (1966).

52. A. Trinquier, J.-L. Birck, C. J. All'egre, High-precision analysis of chromium isotopes in terrestrial and meteorite samples by thermal ionization mass spectrometry. *J. Anal. At. Spectrom.* **23**, 1565–1574 (2008).

53. M. Schiller, E. Van Kooten, J. C. Holst, M. B. Olsen, M. Bizzarro, Precise measurement of chromium isotopes by MC-ICPMS. *JAAS* **29**, 1406–1416 (2014).

54. J. L. Pouchou, F. Pichoir, Quantitative analysis of homogenous or stratified microvolumes applying the model "PAP", in *Electron Probe Quantification*, K. F. J. Heinrich, D. E. Newbury, Eds. (Springer, 1991), pp. 31–75.

55. M. R. Lee, P. A. Bland, G. Graham, Preparation of TEM samples by focused ion beam (FIB) techniques: Applications to the study of clays and phyllosilicates in meteorites. *Min. Mag.* **67**, 581–592 (2003).

56. S. Sridhar, J. F. J. Bryson, A. J. King, R. J. Harrison, Constraints on the ice composition of carbonaceous chondrites from their magnetic mineralogy. *Earth Planet. Sci. Lett.* **576**, 117243 (2021).

57. R. Egli, VARIFORC: An optimized protocol for calculating non-regular first-order reversal curve (FORC) diagrams. *Glob. Planet. Change* **110**, 302–320 (2013).

58. R. Harrison, J. Feinberg, FORCinel: An improved algorithm for calculating first-order reversal curve distributions using locally weighted regression smoothing. *Geochem. Geophys. Geosyst.* **9**, Q05016 (2008).

59. R. Harrison, J. Murszko, D. Heslop, I. Lascu, A. Muxworth, A. Roberts, An improved algorithm for unmixing first-order reversal curve diagrams using principal component analysis. *Geochem. Geophys. Geosyst.* **19**, 1595–1610 (2018).

60. A. J. King, J. R. Solomon, P. F. Schofield, S. S. Russell, Characterising the CI and CI-like carbonaceous chondrites using thermogravimetric analysis and infrared spectroscopy. *Earth Planets Space* **67**, 198 (2015).

61. A. Garenne, P. Beck, G. Montes-Hernandez, R. Chiriac, F. Toche, E. Quirico, L. Bonal, B. Schmitt, The abundance and stability of "water" in type 1 and 2 carbonaceous chondrites (CI, CM and CR). *Geochim. Cosmochim. Acta* **137**, 93–112 (2014).

62. T. Donnelly, S. Waldron, A. Tait, J. Dougans, S. Bearhop, Hydrogen isotope analysis of natural abundance and deuterium-enriched waters by reduction over chromium on-line to a dynamic dual inlet isotope-ratio mass spectrometer. *Rapid Commun. Mass Spectrom.* **15**, 1297–1303 (2001).

63. I. P. Wright, N. J. McNaughton, A. E. Fallick, L. R. Gardiner, C. T. Pillinger, A high-precision mass spectrometer for stable carbon isotope analysis at the nanogram level. *J. Phys. E Sci. Instr.* **16**, 497–504 (1983).

64. I. P. Wright, S. R. Boyd, I. A. Franchi, C. T. Pillinger, High-precision determination of nitrogen stable isotope ratios at the sun-nanomole level. *J. Phys.* **E21**, 865–875 (1988).

65. R. Terborg, A. Kaeppel, B. Yu, M. Patzschke, T. Salge, M. Falke, Advanced chemical analysis using an annular four-channel silicon drift detector. *Microscopy Today* **25**, 30–35 (2017).

66. D. N. Simkus, J. C. Aponte, J. E. Elsila, E. T. Parker, D. P. Glavin, J. P. Dworkin, Methodologies for analyzing soluble organic compounds in extraterrestrial samples: Amino acids, amines, monocarboxylic acids, aldehydes, and ketones. *Life (Basel)* **9**, 47 (2019).

67. D. J. Creek, A. Jankevics, K. E. Burgess, R. Breitling, M. P. Barrett, IDEOM: An excel interface for analysis of LC-MS-based metabolomics data. *Bioinformatics* **28**, 1048–1049 (2012).

68. C. A. Smith, E. J. Want, G. O'Maille, R. Abagyan, G. Siuzdak, XCMS: Processing mass spectrometry data for metabolite profiling using nonlinear peak alignment, matching, and identification. *Anal. Chem.* **78**, 779–787 (2006).

69. R. A. Scheltema, A. Jankevics, R. C. Jansen, M. A. Swertz, R. Breitling, PeakML/mzMatch: A file format, Java Library, R library, and tool-chain for mass spectrometry data analysis. *Anal. Chem.* **83**, 2786–2793 (2011).

70. Y. Gloaguen, F. Morton, R. Daly, R. Gurden, S. Rogers, J. Wandy, D. Wilson, M. Barrett, K. Burgess, PiMP my metabolome: An integrated, web-based tool for LC-MS metabolomics data. *Bioinformatics* **33**, 4007–4009 (2017).

71. J. Xia, N. Psychogios, N. Young, D. S. Wishart, MetaboAnalyst: A web server for metabolomic data analysis and interpretation. *Nucleic Acids Res.* **37**, W652–W660 (2009).

72. D. Vida, P. S. Gural, P. G. Brown, M. Campbell-Brown, P. Wiegert, Estimating trajectories of meteors: An observational Monte Carlo approach—I. Theory. *Mon. Notices Royal Astron. Soc.* **491**, 2688–2705 (2020).

73. P. Spurný, J. Borovička, J. Kac, P. Kalenda, J. Atanackov, G. Kladnik, D. Heinlein, T. Grau, Analysis of instrumental observations of the Jesenice meteorite fall on April 9, 2009. *Meteorit. Planet. Sci.* **45**, 1392–1407 (2010).

74. H. A. R. Devillepoix, E. K. Sansom, P. A. Bland, M. C. Towner, M. Cupák, R. M. Howie, T. Jansen-Sturgeon, M. A. Cox, B. A. D. Hartig, G. K. Benedix, J. P. Paxman, The dingle dell meteorite: A halloween treat from the main belt. *Meteorit. Planet. Sci.* **53**, 2212–2227 (2018).

75. E. K. Sansom, T. Jansen-Sturgeon, M. G. Rutten, H. A. R. Devillepoix, P. A. Bland, R. M. Howie, M. A. Cox, M. C. Towner, M. Cupák, B. A. D. Hartig, 3D meteoroid trajectories. *Icarus* **321**, 388–406 (2019).

76. P. Spurný, J. Borovička, L. Shrbený, The Žďár nad Sázavou meteorite fall: Fireball trajectory, photometry, dynamics, fragmentation, orbit, and meteorite recovery. *Meteorit. Planet. Sci.* **55**, 376–401 (2020).

77. J. Borovička, J. Tóth, A. Igaz, P. Spurný, P. Kalenda, J. Haloda, J. Svoreň, L. Kornoš, E. Silber, P. Brown, M. Husárik, The Košice meteorite fall: Atmospheric trajectory, fragmentation, and orbit. *Meteorit. Planet. Sci.* **48**, 1757–1779 (2013).

78. J. Borovička, P. Spurný, L. Shrbený, Two strengths of ordinary chondritic meteoroids as derived from their atmospheric fragmentation modeling. *Astronom. J.* **160**, 42 (2020).

79. R. J. Macke, G. J. Consolmagno, D. T. Britt, Density, porosity, and magnetic susceptibility of carbonaceous chondrites. *Meteorit. Planet. Sci.* **46**, 1842–1862 (2011).

80. P. M. Schober, E. K. Sansom, P. A. Bland, H. A. R. Devillepoix, M. C. Towner, M. Cupák, R. M. Howie, B. A. D. Hartig, S. L. Anderson, The main asteroid belt: The primary source of debris on comet-like orbits. *Planet. Sci. J.* **2**, 98 (2021).

81. H. Rein, D. S. Spiegel, IAS15: A fast, adaptive, high-order integrator for gravitational dynamics, accurate to machine precision over a billion orbits. *MNRAS* **446**, 1424–1437 (2015).

82. C. M. Pieters, L. A. Taylor, S. K. Noble, L. P. Keller, B. Hapke, R. V. Morris, C. C. Allen, D. S. McKay, S. Wentworth, Space weathering on airless bodies: Resolving a mystery with lunar samples. *Meteorit. Planet. Sci.* **35**, 1101–1107 (2000).

83. H. C. Bates, A. J. King, K. L. Donaldson Hanna, N. E. Bowles, S. S. Russell, Linking mineralogy and spectroscopy of highly aqueously altered CM and CI carbonaceous chondrites in preparation for primitive asteroid sample return. *Meteorit. Planet. Sci.* **55**, 77–101 (2020).

84. H. Busemann, H. Baur, R. Wieler, Primordial noble gases in “phase Q” in carbonaceous and ordinary chondrites studied by closed system stepped etching. *Meteorit. Planet. Sci.* **35**, 949–973 (2000).

85. G. R Huss, R. S. Lewis, Noble gases in presolar diamonds I: Three distinct components and their

implications for diamond origins. *Meteoritics* **29**, 791–810 (1994).

86. I. Leya, J. Masarik, Cosmogenic nuclides in stony meteorites revisited. *Meteorit. Planet. Sci.* **44**, 1061–1086 (2009).

87. C. M. O'D. Alexander, Quantitative models for the elemental and isotope fractionation in chondrites: The carbonaceous chondrites. *Geochim. Cosmochim. Acta* **254**, 277–309 (2019).

88. N. Bhandari, S. V. S. Murty, P. N. Shukla, A. D. Shukla, R. R. Mahajan, M. M. Sarin, G. Srinivasan, K. M. Suthar, M. S. Sisodia, S. Jha, A. Bischoff, Itawa Bhopji (L3-5) chondrite regolith breccia: Fall, classification and cosmogenic records. *Meteorit. Planet. Sci.* **37**, 549–563 (2002).

89 P. P. Povinec, J. Masarik, I. Sýkora, A. Kováčik, J. Beňo, M. Laubenstein, V. Porubčan, Cosmogenic nuclides in the Košice meteorite: Experimental investigations and Monte Carlo simulations. *Meteorit. Planet. Sci.* **50**, 880–892 (2015).

90. N. Braukmüller, F. Wombacher, D. C. Hezel, R. Escoube, C. Münker, The chemical composition of carbonaceous chondrites: Implications for volatile element depletion, complementarity and alteration. *Geochim. Cosmochim. Acta* **239**, 17–48 (2018).

91. M. S. Spergel, R. C. Reedy, O. W. Lazareth, P. W. Levy, L. A. Slatest, Cosmogenic neutron-capture-produced nucleides in stony meteorites. *J. Geophys. Res. Suppl.* **91**, D483–D494 (1986).

92. R. Wieler, T. Graf, P. Signer, S. Vogt, G.F. Herzog, C. Tuniz, D. Fink, L. K. Fifield, J. Klein, R. Middleton, A. J. T. Jull, P. Pellas, J. Masarik, G. Dreibus, Exposure history of the Torino meteorite. *Meteorit. Planet. Sci.* **31**, 265–272 (1996).

93. G. F. Herzog, Cosmic-ray exposure ages of meteorites, in *Treatise on Geochmistry*, H. D. Holland, K. K. Turekian, Eds. (Elsevier, 2003), vol. 1.

94. T. Schulz, P. P. Povinec, L. Ferrière, A. J. T. Jull, A. Kováčik, I. Sýkora, J. Tusch, C. Münker, D. Topa, C. Koeberl, The history of the Tissint meteorite, from its crystallization on Mars to its exposure in space: New geochemical, isotopic, and cosmogenic nuclide data. *Meteorit. Planet. Sci.* **55**, 294–311 (2020).

95. K. T. Howard, C. M. O'D. Alexander, D. L. Schrader, K. Dyl, Classification of hydrous meteorites (CR, CM and C2 ungrouped) by phyllosilicate fraction: PSD-XRD model mineralogy and planetesimal environments. *Geochim. Cosmochim. Acta* **149**, 206–222 (2015).

96. M. R. Lee, P. Lindgren, M. R. Sofe, Aragonite, breunnerite, calcite and dolomite in the CM carbonaceous chondrites: High fidelity recorders of progressive parent body aqueous alteration. *Geochim. Cosmochim. Acta* **144**, 126–156 (2014).

97. D. J. Barber, Phyllosilicates and other layer-structured materials in stony meteorites. *Clay Miner.* **20**, 415–454 (1985).

98. I. D. R. Mackinnon, M. E. Zolensky, Proposed structures for poorly characterized phases in C2M carbonaceous chondrite meteorites. *Nature* **309**, 240–242 (1984).

99. P. Rochette, J. Gattacceca, L. Bonal, M. Bourot-Denise, V. Chevrier, J. Clerc, G. Consolmagno, L. Folco, M. Gounelle, T. Kohout, L. Pesonen, E. Quirico, L. Sagnotti, A. Skripnik, Magnetic classification of stony meteorites: 2. Non-ordinary chondrites. *Meteorit. Planet. Sci.* **43**, 959–980 (2008).

100. C. Cournède, J. Gattacceca, M. Gounelle, P. Rochette, B. Weiss, B. Zanda, An early solar system magnetic field recorded in CM chondrites. *Earth Planet. Sci. Lett.* **410**, 62–74 (2015).

101. R. Harrison, I. Lascu, FORCulator: A micromagnetic tool for simulating first-order reversal curve diagrams. *Geochem. Geophys. Geosyst.* **15**, 4671–4691 (2014).

102. R. Harrison, X. Zhao, P. Hu, T. Sata, D. Heslop, A. Muxworthy, H. Oda, V. Kuppili, A. Roberts, Simulation of remanent, transient, and induced first-order reversal curve (FORC) diagrams for interacting particles with uniaxial, cubic, and hexagonal anisotropy. *J. Geophys. Res. Solid Earth* **124**, 1404–1429 (2019).

103. J. Bryson, B. Weiss, J. Biersteker, A. King, S. Russell, Constraints on the distances and timescales of solid migration in the early solar system from meteorite magnetism. *Astrophys. J.* **869**, 103 (2020).

104. J. Bryson, B. Weiss, E. Lima, J. Gattacceca, W. Cassata, Evidence for asteroid scattering and distal solar system solids from meteorite paleomagnetism. *Astrophys. J.* **892**, 126 (2020).

105. V. K. Pearson, M. A. Sephton, I. A. Franchi, J. M. Gibson, I. Gilmour, Carbon and nitrogen in carbonaceous chondrites: Elemental abundances and stable isotopic compositions. *Meteorit. Planet. Sci.* **41**, 1899–1918 (2006).

106. C. M. O'D. Alexander, S. S. Russell, J. W. Arden, R. D. Ash, M. M. Grady, C. T. Pillinger, The origin of chondritic macromolecular matter: A carbon and nitrogen isotope study. *Meteorit. Planet. Sci.* **33**, 603–622 (1998).

107. S. S. Russell, J. W. Arden, C. T. Pillinger, A carbon and nitrogen isotope study of diamond from primitive chondrites. *Meteorit. Planet. Sci.* **31**, 343–355 (1996).

108. M. M. Grady, I. P. Wright, P. K. Swart, C. T. Pillinger, The carbon and oxygen isotopic composition of meteoritic carbonates. *Geochim. Cosmochim. Acta* **52**, 2855–2866 (1988).

109. M. M. Grady, A. B. Verchovsky, I. A. Franchi, I. P. Wright, C. T. Pillinger, Light dement geochemistry of the Tagish Lake CI2 chondrite: Comparison with CI1 and CM2 meteorites. *Meteorit. Planet. Sci.* **37**, 713–735 (2002).

110. M. A. Sephton, Organic geochemistry of meteorites, in *Treatise on Geochmistry* (Elsevier, ed. 2, 2014), vol. 1, chap. 12.

111. M. A. Sephton, A. B. Verchovsky, P. A. Bland, I. Gilmour, M. M. Grady, I. P. Wright, Investigating the variations in carbon and nitrogen isotopes in carbonaceous chondrites. *Geochim. Cosmochim. Acta* **67**, 2093–2108 (2003).

112. E. Mazor, D. Heymann, E. Anders, Noble gases in carbonaceous chondrites. *Geochim. Cosmochim. Acta* **34**, 781–824 (1970).

113. A. Boosman, I. L. ten Kate, P. Mason, L. Polerecky, D. Materic, R. Hilzinger, T. Rockmann, UV induced methane and volatile organic carbon emission from the Murchison meteorite. *EPSC Abstr.* **12**, EPSC2018-663 (2018).

114. J. G. Lawless, G. U. Yuen, Quantification of monocarboxylic acids in the Murchison carbonaceous meteorite. *Nature* **282**, 396–398 (1979).

115. G. W. Cooper, W. M. Onwo, J. R. Cronin, Alkyl phosphonic acids and sulfonic acids in the Murchison meteorite. *Geochim. Cosmochim. Acta* **56**, 4109–4115 (1992).

116. D. P. Glavin, J. P. Dworkin, A. Aubrey, O. Botta, J. H. Doty III, Z. Martins, J. L. Bada, Amino acid analyses of Antarctic CM2 meteorites using liquid chromatography-time of flight-mass spectrometry. *Meteorit. Planet. Sci.* **41**, 889–902 (2006).

117. V. S. Heber, R. Wieler, H. Baur, C. Olinger, D. Burnett, Noble gas composition of the solar wind as collected by the Genesis mission. *Geochim. Cosmochim. Acta* **73**, 7414–7432 (2012).

118. D. Györe, A. Tait, D. I. Hamilton, F. M. Stuart, The formation of NeH^+ in static vacuum mass spectrometers and re-determination of $^{21}Ne/^{20}Ne$ of air. *Geochim. Cosmochim. Acta* **263**, 1–12 (2019).

119. R. Wieler, Cosmic ray-produced noble gases in meteorites. *Rev. Mineral. Geochem.* **47**, 125–170 (2002).

120. N. Dauphas, The isotopic nature of the Earth's accreting material through time. *Nature* **541**, 521–524 (2017).

120. A. Meshik, C. Hohenberg, O. Pravdivtseva, D. Burnett, Measuring the isotopic composition of solar wind noble gases, in *Exploring the Solar Wind*, M. Lasar, Ed. (2012), pp. 93–121.

121. R. Wieler, E. Anders, H. Baur, R. S. Lewis, P. Signer, Characterisation of Q-gases and other noble gas components in the Murchison meteorite. *Geochim. Cosmochim. Acta* **56**, 2907–2921 (1992).